Astronomy & Astrophysics manuscript no. output
May 5, 2026

Robust active galactic nucleus and host-galaxy decomposition in optical spectral fitting

C. Aydar[1,2⋆], A. Merloni[1], G. Zeltyn[3], C. Andonie[1], B. Trakhtenbrot[3], S. Bernal[4,5], Q. Wu[6], J. Buchner[1], M. Salvato[1], T. Dwelly[1], S. F. Anderson[7], R. J. Assef[8], F. E. Bauer[9], W. N. Brandt[10,11,12], S. LaMassa[13], M. L. Martínez-Aldama[14], A. L. Rankine[15], D. P. Schneider[10,16], Y. Shen[6,17], J. R. Brownstein[18], H. Javier Ibarra-Medel[19], A. M. Koekemoer[13], M. Krumpe[20], S. Morrison[6], K. Nandra[1], C. A. Negrete Peñaloza[19], and S. F. Sanchez[21]

(Affiliations can be found after the references)

ABSTRACT

Unraveling the growth of supermassive black holes and their connection to host galaxies requires disentangling the active galactic nuclei (AGN) emission from that of the stellar populations in which they are embedded. When an AGN spectrum is observed at different activity phases, if the spectral decomposition properly recognizes the nuclear and stellar components, key physical properties — such as black hole mass, stellar mass, and stellar velocity dispersion — should remain consistent. These quantities are essential for scaling relations used to study the co-evolution of black holes and galaxies. We present a novel optical spectral-fitting approach that combines `pPXF` and `PyQSOFit` to robustly decompose spectra into stellar and AGN components. We applied this technique to three Sloan Digital Sky Survey samples with repeated optical spectra of the same objects at $z \leq 0.55$: 32 changing-look AGN in bright and dim states and 15 quasars and 15 galaxies with three single-epoch and one stacked spectrum each and spanning a range of signal-to-noise ratios. For comparison with the literature, we also used SDSS spectra and photometric data from AGN in the eFEDS field as well as Gemini and VLT observations of some of our selected changing-look AGN. This analysis enabled us to evaluate the reliability of stellar mass, velocity dispersion, and black hole mass measurements, especially in relation to the AGN-to-total continuum contribution ($f_{\rm AGN}$). For host-derived properties, especially when $f_{\rm AGN} < 0.8$, our method yields consistent results. For single-epoch black hole mass estimates from Hα and Hβ, a 3σ confidence in the broad-line flux and full width at half maximum provides effective criteria for selecting reliable measurements. The reliability of our measurements was confirmed by their alignment with previously established scaling relations. Many changing-look AGN in our sample exhibit "breathing" broad-line regions, as determined from Hα analysis, while some deviate significantly, suggesting non-virialized systems across the spectral transition.

Key words. galaxies: active - galaxies: evolution - quasars: emission lines - techniques: optical spectroscopy

1. Introduction

Active galactic nuclei (AGN) represent a phase in the evolution of galaxies during which their central supermassive black hole (SMBH) accretes matter and grows its mass. Very energetic processes occur during the AGN phase, and their impact on the host galaxy has been studied in both simulations and observations alike (see Fabian 2012; Harrison & Ramos Almeida 2024 for a review). Scaling relations that correlate properties of the SMBH with properties of the host-galaxy and its bulge indicate a possible co-evolution of these systems (e.g., Magorrian et al. 1998; Gebhardt et al. 2000; Graham et al. 2001; Tremaine et al. 2002; Kormendy & Ho 2013) that is driven by feedback from the AGN driving outflows, jets, and winds that can interact with the galaxy up to scales that are much larger than the SMBH sphere of influence (e.g., Fabian 2012; Förster Schreiber et al. 2014; Morganti 2017). Studies with high spatial resolution have been crucial for mapping the influence of outflows and jets in the interstellar medium to either enhance or suppress star formation in the galaxy as a consequence of the SMBH activity (e.g., Balmaverde et al. 2019; Venturi et al. 2021; Riffel et al. 2023a,b; Speranza et al. 2024).

However, when the AGN is not observed with sufficient spatial resolution (e.g., in single-epoch fiber-fed spectroscopy), it is crucial to disentangle the host galaxy and AGN emission in the combined spectra to determine their respective contributions. Due to the advent of large spectroscopic surveys such as the Sloan Digital Sky Survey (SDSS; York et al. 2000; Kollmeier et al. 2026) and especially considering the new generation of big data from, for example, the Dark Energy Spectroscopic Instrument (DESI; DESI Collaboration et al. 2026), the 4-metre Multi-Object Spectroscopic Telescope (4MOST; de Jong et al. 2019), and the Prime Focus Spectrograph (PFS; Tamura et al. 2016), it is necessary to have a reliable method to separate the emission from the stellar populations in the galaxy from the emission from the growth of the SMBH in the large samples of fiber-fed spectra that are and will be available to the scientific community. Part of the challenges in developing a method applicable in an automated way to thousands or even millions of spectra is the variety of AGN spectra, considering the diversity in obscuration, accretion rate, and AGN luminosity, as well as the influence of the stellar populations (e.g., Aydar et al. 2025). With the long-term objective of being able to analyze large samples of AGN selected in different ways as part of the SDSS-V Black Hole Mapper (BHM) program (Kollmeier et al. 2026), the specific goal of this paper is to devise and validate a flexible and robust optical fitting method and to test its performance on a set of SDSS spectra.

To test the reliability of the results of the fitting method, one could use mock samples, in which the fit measurements should match the input parameters that generated the spectra (e.g., Santini et al. 2012; Mobasher et al. 2015; Buchner et al. 2024). This approach, however, can be highly biased due to its dependence on the templates used to construct the mock spectra,

⋆ caydar@mpe.mpg.de

Article published by EDP Sciences, to be cited as https://doi.org/10.1051/0004-6361/202558027

and it becomes unrealistic when comparing the test to observed data, given the difficulty of realistically applying noise (e.g., Bongiorno et al. 2012). However, observational data can be used to assess the quality of a fitting model, as observing the same galaxy at different phases of its activity across various signal-to-noise ratios or with different telescopes should yield the same output measurements.

We therefore selected samples of AGN observed multiple times with SDSS: one sample of "changing-look" AGN (CL-AGN, see Ricci & Trakhtenbrot 2023, for a recent review) in their bright and dim states and two other samples that allow for comparison of single-epoch and stacked spectra of the same source for (X-ray-selected) AGN. For each object in these samples, some parameters should remain constant, such as galaxy stellar mass, stellar velocity dispersion, and black hole mass, as we do not expect them to vary on such short timescales. These quantities are also often used in the scaling relations to understand the possible co-evolution of AGN and their hosts (e.g., Kormendy & Ho 2013; Reines & Volonteri 2015; Suh et al. 2020; Pucha et al. 2025).

This paper primarily focuses on validating the proposed methodology. However, the method can also yield many relevant physical parameters for studying either the AGN or their host galaxies, as it provides continuum, emission, and absorption line measurements separately for each component.

The structure of the paper is as follows. In Section 2 we describe the methodology for fitting the spectra with the host galaxy and AGN decomposition. The samples used for validating this method are presented in Section 3. Section 4 presents the method validation, for which we compared the outputs of different spectra of the same objects (internal validation) and the results of our method with analysis from photometric fitting (external validation), with a focus on host galaxy properties (stellar mass and stellar velocity dispersion) and on AGN properties (SMBH mass). Our results are discussed in the context of scaling relations and "breathing" broad-line regions (BLRs) in Section 5, and the paper concludes with recommendations for the use of the fitting method in Section 6. Throughout this paper, we assume a flat Lambda cold dark matter cosmology with $\Omega_M = 0.3$ and $H_0 = 70$ km s^{-1} Mpc^{-1}.

2. Methodology

The goal of this work is to provide and validate a reliable method for fitting the contribution of AGN and the host galaxies in optical spectra where both sources of emission are entangled. Our strategy is to accurately remove the host-galaxy contribution from the observed spectra, and then fit the residual AGN-dominated spectrum with a procedure optimized to account for the AGN continuum and emission lines. Importantly, removing the host galaxy with high precision enabled us to study the properties of even weak emission lines in greater detail, which would otherwise be blended with stellar emission.

To obtain accurate measurements of both the host galaxy emission and the AGN, we used two software packages, developed with a focus on either inactive galaxies or quasars. We used `pPXF` (Cappellari 2023) for modeling the stellar populations (while still adding the AGN components to avoid overestimates and to account for known degeneracies, e.g., Tadhunter et al. 1996; Stasińska et al. 2006) and `PyQSOFit` (Guo et al. 2018) for fitting the AGN emission. `pPXF` was primarily built to focus on low-redshift inactive galaxies, and the adaptations made to the code to account for the AGN emission are not as complex as the fit from `PyQSOFit`. On the other hand, `PyQSOFit` was built with a focus on quasars, and its host galaxy subtraction option often fails to provide accurate fits when accounting for both AGN and stellar populations. For these reasons, we decided to combine the best aspects of both codes to achieve a reliable decomposition of AGN and host galaxies. We performed three iterations of the fits with different model components for each spectrum to obtain a trustworthy AGN and host-galaxy decomposition, as described in the following sections. Regarding computational efficiency, a complete run with both `pPXF` and `PyQSOFit` on a single CPU core takes ~ 3 minutes for each SDSS spectrum.

2.1. pPXF

The code `pPXF` (Cappellari 2023, and references therein) is a `Python` implementation of the Penalized Pixel-Fitting method for spectral fitting. It fits the observed spectrum with a set of stellar population templates and associated kinematic components to extract the stellar and gas kinematics, as well as the properties of the predominant stellar populations. `pPXF` was originally built to fit the spectra of inactive galaxies; hence, we used it only to obtain information regarding the stellar populations of the host galaxy (e.g., stellar velocity dispersion, stellar mass, and stellar population age and metallicity), and not to obtain the AGN measurements. Following Bernal et al. (2025), we adapted the algorithm to also model AGN in their bright states, where the host galaxy's emission is partly outshone by the quasar. Figure 1 shows the templates used in our fitting procedure with `pPXF`: power-law featureless continuum, stellar populations, Fe II pseudo-continuum (in the figure we display only the example with full width at half maximum FWHM = 4000 km s^{-1}), Balmer continuum and high-order emission, broad emission lines, and narrow emission lines.

For our implementation of `pPXF`, we used simple stellar populations (SSPs) from E-MILES (Vazdekis et al. 2016) with Padova isochrones (Girardi et al. 2000) and a Salpeter (1955) initial mass function. We adopted a model grid with $\log(t/yr) = 7.8 - 10.2$ in 0.1 dex steps, with the metallicities of -1.71, -1.31, -0.71, -0.4, 0.0, 0.22 in [M/H] (in which 0.0 corresponds to solar metallicity). The stellar component had four kinematic moments, with the velocity ranging from -300 to 500 km s^{-1}, the velocity dispersion from 10 to 500 km s^{-1}, and the skewness and kurtosis varied from -0.3 to 0.3. The description and references for the fitting of the continuum are also described in Table A.1.

To account for the emission lines in the AGN spectrum, we added templates with Gaussians for the narrow and broad lines. For the narrow lines, we included the Balmer lines in the optical domain (Hα, Hβ, Hγ, and Hδ), [S II], [N II], [O I], [O II], [O III], [Ne III], and [Ne V] optical doublets, He I, and Mg II. The velocity offset range of the narrow emission lines was -800 to 500 km s^{-1}, with velocity dispersion from 1 to 300 km s^{-1}. For the broad lines, we considered Gaussians with broader components for the Balmer lines, He I, and Mg II, with velocities ranging from -500 to 300 km s^{-1} and velocity dispersions from 400 to 10000 km s^{-1}. We considered a simplified approach of tidying all narrow lines fit with a single Gaussian and a similar approach for the broad lines, since more complex fitting would be provided by `PyQSOFit`. The emission line fitting before the host-galaxy decomposition is not accurate, so the `pPXF` fit of the lines is only used to guarantee the self-consistency of the fit in each iteration.

We also included components to account for the AGN contribution to the continuum. We generated featureless power-law continua with

$$f_\lambda(\lambda) = f_\lambda(\lambda_0) \left(\frac{\lambda}{\lambda_0}\right)^\alpha ,$$

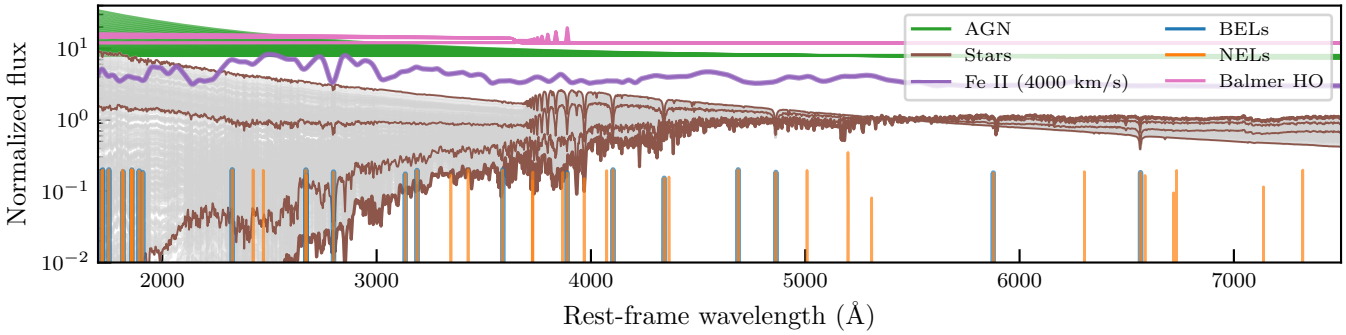

Fig. 1. Templates used in pPXF fits to prepare for the galaxy subtraction. The power-law continuum (AGN) is displayed in green, with different power-law indices. The E-MILES stellar populations (Stars) are shown in gray, with some of the SSPs highlighted in brown. The Fe II component (broadened with a 4000 km s^{-1} FWHM, as an example) is shown in purple. The Balmer continuum and higher-order emission (Balmer HO) are shown in pink. The wavelengths of the broad emission lines (indicated as BELs) are shown in blue, those of the narrow emission lines (indicated as NELs) in orange; they often overlap for lines that have both such components. Except for the SSPs, each template is displayed in a different normalization for visualization purposes.

with α varying from -3.0 to 0.0 in steps of 0.1. The Balmer continuum emission templates had an optical depth range τ from 0.1 to 2.0 in steps of 0.1, while the Balmer High Order templates had FWHM from 1000 to 11000 km s^{-1}. The velocity offset of the Balmer emission was tied to that of the broad emission lines.

The Fe II pseudo-continuum templates used were a combination of those by Boroson & Green (1992) for optical wavelengths and by Vestergaard & Wilkes (2001) for ultraviolet wavelengths. We broadened such templates with different values of the FWHM: 1000, 1200, 1400, 1600, 1800, 2000, 2400, 2800, 3400, 4000, 4800, 5800, 7000, 8400, 10000, and 11800 km s^{-1} as in Bernal et al. (2025).

The approach to add the appropriate Balmer- and Fe II pseudo-continuum templates required running pPXF (at least) twice. In the first run, we considered all other components of the fit (i.e., SSPs, broad and narrow emission lines, and the power-law continuum) without including the Balmer and Fe II templates; in particular, we obtained a first estimate of the broad line kinematic width from this run. Then, we selected the Balmer High-Order and Fe II templates that were broadened to the closest value of the broad-line width, assuming the two are dynamically linked in the BLR of the AGN (e.g., Barth et al. 2013; Ji et al. 2025). In subsequent runs, with the broadened Balmer- and Fe II pseudo-continua and the other components included in the fit, we confirmed that the model converged. For all the spectra considered here, only one iteration was enough to reach convergence between the width of the broad emission line component and the Balmer High Order and Fe II templates.

For the fit of the observed spectra, we first performed the de-reddening of the observed flux due to the Milky Way extinction using the dust map from Schlegel et al. (1998) and the adapted values based on SDSS from Schlafly & Finkbeiner (2011), and the Cardelli et al. (1989) extinction curve with $R_V = 3.1$. Then, we set the spectra to the rest frame using the SDSS pipeline redshift. To estimate the uncertainties associated with our measurements, we performed Monte Carlo iterations by adding random noise within each pixel's noise range. The provided estimates and statistical uncertainties correspond to the mean and standard deviations of 25 iterations.

Figure 2 shows an example of a pPXF fit. Our primary focus is on the output associated with the stellar populations, which is displayed as the brown component. pPXF provides the weight of the linear combination of the templates used for the fit. From the weight of the AGN emission (the sum of the weights of the power-law, the Fe II, and the Balmer continuum and high-order emission) in comparison to the contribution of the SSPs to the continuum, we estimated the fraction of the AGN emission for each spectrum, which will be referred to as AGN continuum contribution ($f_{\rm AGN}$). Since this measurement encompasses the entire wavelength range, it is also affected by redshift.

From the SSP kinematic components, we obtained the stellar velocity dispersion (σ_*) from the best-fitting line-of-sight velocity distribution returned by pPXF, which is mainly constrained by prominent absorption features (e.g., Ca H+K, Mg I b). The output also provided the ages and metallicities of the stellar populations, weighted by both mass and light. We also estimated the aperture stellar masses ($\overline{M}_*$), i.e., the stellar mass obtained by the spectral fitting without aperture corrections, which corresponds to a lower limit of the stellar mass of the galaxy. Having derived the properties of the host's stellar populations (e.g., stellar mass, stellar velocity dispersion, stellar population age and metallicity, weights for each SSP template), we subtracted the SSP templates from the de-reddened observed spectrum to obtain the isolated AGN emission.

2.2. PyQSOFit

After the host-galaxy contribution was properly measured and subtracted from the observed spectra, we fit the isolated AGN emission using PyQSOFit (Guo et al. 2018). PyQSOFit was designed to fit the optical spectra of SDSS quasars, and it includes Monte Carlo estimates of the uncertainties of the fitting results, with a similar setting of 25 runs that was implemented in pPXF. PyQSOFit provides a fit for each model component, rather than a linear combination as pPXF, and this complexity yields more accurate results for the AGN component.

We used a similar approach to the one described in Wu & Shen (2022). For the continuum, we fitted a combination of a power-law and a third-order polynomial to account for objects with intrinsic dust reddening associated with the AGN environment rather than the host galaxy. The flexibility of the polynomial fit also includes the contributions of the Balmer continuum and higher-order emission. We also included Fe II pseudo-continuum templates, but this time the width of the line complexes was fit to the spectrum instead of approximating a FWHM as for the

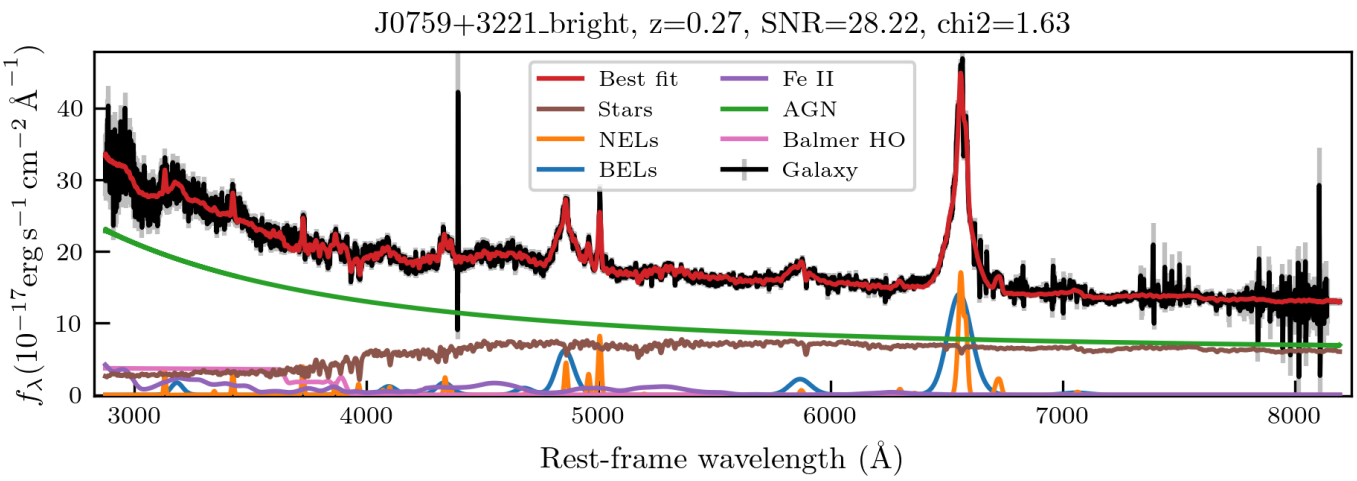

Fig. 2. Example `pPXF` fit. The templates are color coded as in Fig. 1, with the observed spectra in black and the overall fit in red. This fit is an example of a successful decomposition of the host galaxy (brown) and the continuum components of the AGN (green, pink, and purple).

`pPXF` fit. We used the Fe II template provided by `PyQSOFit`, which is a combination of the templates from Boroson & Green (1992), Vestergaard & Wilkes (2001), Tsuzuki et al. (2006), and Salviander et al. (2007). There is, however, a gap in the Fe II models in the wavelength range $\sim$ 3490 – 3730 Å, which is the result of missing high-order Balmer lines and the Balmer edge at 3646 Å (see, e.g., Park et al. 2022). The parameters and references for the fitting of the AGN continuum by `PyQSOFit` are also listed in Table A.2.

The emission lines were fit with 1 to 3 Gaussians per line, with the parameters listed in Table A.3 and further discussed in Appendix A. Using several Gaussians with more constrained parameters is very important to avoid misleading estimates, since we are able to disentangle lines that could be blended, such as [N II] and [S II] from Hα (see the middle right panel of Fig. 3). Regarding the subtraction of absorption lines from the SSP contribution, no significant dip was noticed in the visual inspection of the Balmer line profiles in our fits, indicating that the absorption lines are accounted for consistently with the host galaxy templates and do not significantly affect the emission lines.

From these fits, we obtained the main properties of the AGN. Figure 3 displays an example of the `PyQSOFit` fit to the same spectrum as in Fig. 2 after its host-galaxy subtraction. The lower panel of Fig. 3 shows the fits for faint lines, and although they were measured, some quality cuts as recommended by Wu & Shen (2022) should be applied before considering them a reliable detection. We emphasize the importance of measuring AGN emission lines after decomposing the host-galaxy contribution to obtain unbiased physical parameters of SMBH activity.

3. Samples

In this section, we describe the samples used to test and validate our method; all are based on SDSS optical spectra. In Section 3.1, we present three samples of spectra selected for comparing different observations of the same objects for an internal validation of our methodology. Section 3.2 instead presents four samples from the eFEDS field for the comparison of our method with results from other AGN/host decomposition methods that rely on photometry and either spectral energy distribution (SED) fitting or image decomposition. At last, Section 3.3 presents the VLT and Gemini spectra used to compare the stellar velocity dispersion measurements.

The Sloan Digital Sky Survey has provided optical spectra of all types of astronomical objects since its first generation (York et al. 2000) to the most recent release (SDSS Collaboration et al. 2025). The SDSS-I and II performed their observations using a spectrograph (Smee et al. 2013) with 3" (diameter) fibers (York et al. 2000; Eisenstein et al. 2001; Strauss et al. 2002; Gunn et al. 2006; Abazajian et al. 2009). SDSS-III introduced the Baryon Oscillation Spectroscopic Survey (BOSS, Eisenstein et al. 2011; Dawson et al. 2013) spectrographs using 2" (diameter) fibers. The survey migrated from the plate design to robotic fibers during SDSS-V, while using the same spectrographs (Blanton et al. 2017; Abdurro'uf et al. 2022), and the ongoing generation SDSS-V (Kollmeier et al. 2026) has already announced two data releases (Almeida et al. 2023; SDSS Collaboration et al. 2025), with the next data release also including targets in the Southern Hemisphere using the LCO 2.5-m telescope (Bowen & Vaughan 1973), with a 1.3" (diameter) fiber.

3.1. Internal comparison

For internal comparison, i.e., comparing different observations of the same sources, we constructed three custom-made small samples of SDSS AGN data. The legacy of decades of SDSS observations is crucial for this analysis, as it allows for comparison of data from the same source across years. This enables, in particular, the analysis of objects that might have changed their emission profile. For most spectra, we used the `idlspec2d` pipeline version of SDSS (Bolton et al. 2012; Dawson et al. 2013; Morrison et al. in prep.).

The sample CL consists of 32 changing-look AGN: 20 selected from Zeltyn et al. (2024) and 12 newly identified CL-AGN (Zeltyn et al. 2026) from SDSS-V (Kollmeier et al. 2026). Two spectra are associated with each AGN, corresponding to their bright (usually quasar-dominated phase, with broad Hα and a power-law continuum) and dim (typically host-galaxy-dominated, as seen from absorption lines and a continuum shape consistent with stellar populations, with narrower emission lines) states. By selection, there is often a significant dimming of the broad Hβ emission between the bright and dim states. The redshift range of the sources is $0.05 \leq z \leq 0.5$.

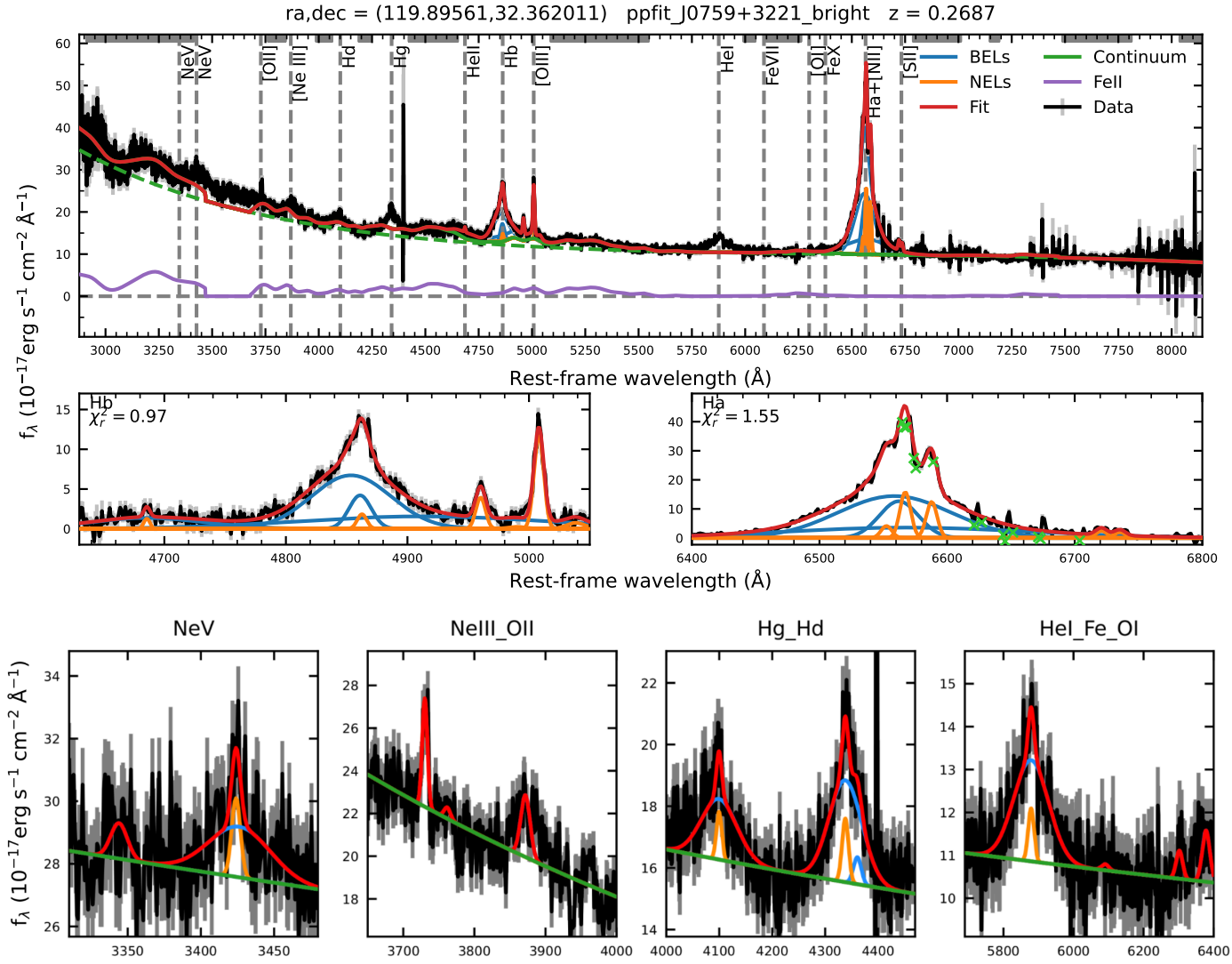

Fig. 3. Fit from `PyQSOFit` of the same spectrum as in Fig. 2 after the subtraction of the host galaxy. The top panel shows the overall fit in red over the data in black. The middle panels display the fits for the Hα and Hβ complexes, and the bottom panels present the fits for other emission lines that were treated locally due to being fainter. The colors of the templates are as in Fig. 1. The gray bands at the top indicate the wavelength regions considered for the continuum fit.

We also defined two more samples, GAL and QSO, each with 15 AGN detected by eROSITA (Predehl et al. 2021; Merloni et al. 2024) that the SDSS pipeline classified as `GALAXY` and `QSO`, respectively (see the SDSS DR19 Value Added Catalog in SDSS Collaboration et al. 2025). While the `QSO` class clearly indicates that the AGN is unobscured, the classification as `GALAXY` indicates the presence of features typical of galaxies, though their point-like X-ray detection suggests the presence of an AGN. Each source has three spectra from co-added observations (regular observations typically taken within one day) and one stacked spectrum that combines all SDSS observations of this object (from 2020 to 2025), referred to as `daily` and `allepoch`, respectively. The `daily` spectra of each source comprise a median S/N range through all spectra (`SN_MEDIAN_ALL`) of $3.16 < S/N < 5$, $5 \leq S/N < 10$, and $S/N \geq 10$. Unless the S/N bin is explicitly specified, we present results for all S/N ranges. The sources have $0.02 \leq z \leq 0.55$ and no SDSS pipeline flag indicating a problematic redshift (`ZWARNING`= 0). For both samples, we aimed to select cases in which both host-galaxy and AGN contributions would be present: for sample GAL, we gave preference to spectra with `SUBCLASS` containing keywords as `AGN` or `BROADLINE`, while for sample QSO, we prioritized keywords as `STARFORMING` or `STARBURST`.

With this sample selection, we have a total of 184 spectra (64 CL, 60 GAL, and 60 QSO) from 62 sources (32 CL, 15 GAL, and 15 QSO), spanning different host-galaxy versus AGN contributions and different S/N. Figure 4 shows the different generations of SDSS spectra that were considered in our three samples with regard to their luminosities (our measurement of L_{5100} and bolometric luminosity according to Runnoe et al. 2012) and f_{AGN}. The value of L_{5100} was estimated from the average flux at 5080-5120 Å and the SDSS pipeline redshift. The sample CL spans different generations of SDSS, with a similar range of luminosities ($\langle \log(L_{5100}/\mathrm{erg\ s^{-1}}) \rangle = 43.9 \pm 0.3$ for the bright sample, 43.7 ± 0.3 for the dim sample). For most sources in the CL sample, the first observation is brighter than the second. Sample GAL shows slightly lower luminosities ($\langle \log(L_{5100}/\mathrm{erg\ s^{-1}}) \rangle = 43.6 \pm 0.3$), as expected for a sample of narrow-line AGN compared to broad-line AGN (e.g., Koss et al. 2017; Barquín-González et al. 2024). Though the QSO sample

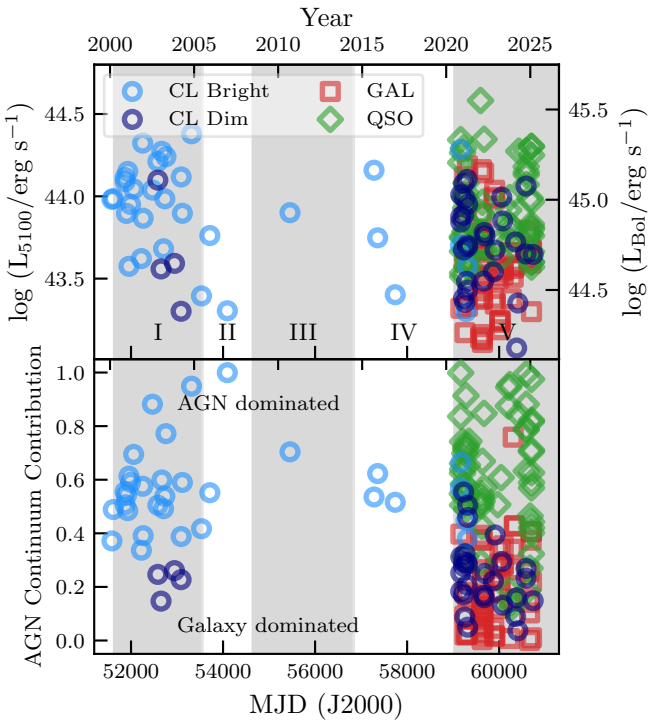

Fig. 4. *Top panel:* Observed luminosity at 5100 Å (left axis) and bolometric luminosity (right axis) vs. time of observation for all the spectra analyzed in this work. *Bottom panel:* Fraction of the AGN emission ($f_{\rm AGN}$) as derived from the `pPXF` decomposition vs. Modified Julian Date. The sample CL is indicated in light blue and dark blue circles for spectra taken during the bright and dim stages of the AGN, respectively. Sample GAL is shown in red squares and sample QSO in green diamonds. For reference, the various SDSS generations are represented by gray or white shaded areas, with numbers I-V as indicators.

has the spectra with the highest luminosities, the mean luminosity is the same as that of sample CL ($\langle \log(L_{5100}/\mathrm{erg\ s^{-1}}) \rangle$ = 43.9 ± 0.3). These similar average luminosities are due to their (X-ray) selection, which suggests that an AGN component is present, and the construction of SDSS subclasses that indicate star formation for the QSO sample and AGN activity in the GAL sample. Interestingly, most bright CL AGN and QSO have AGN continuum contribution $f_{\rm AGN}$>0.4, while the GAL and dim CL states are mostly $f_{\rm AGN}$<0.4, as expected.

3.2. Testing against external samples: Stellar mass

To compare the results of our methodology with other works in the literature, we decided to use the eROSITA Final Equatorial Depth Survey field (eFEDS; Brunner et al. 2022), which provides extensive multi-wavelength coverage. Out of the 28k X-ray point-like sources detected in eFEDS with eROSITA, 13k were followed up with SDSS as part of the SPectral IDentification of ERosita Sources program (SPIDERS; Dwelly et al. 2017; Aydar et al. 2025). After removing ∼ 3% of stars and doing some quality cuts for guaranteeing reliable counterparts and redshift, we applied our spectral-fitting method to sources at z< 1 that were either red ($g - r > 0.4$) or extended according to the Legacy Survey (Dey et al. 2019), which corresponded to 3702 AGN candidates of having a significant host galaxy (compared to the total eFEDS-SPIDERS sample of 12 847 AGN; Aydar et al., in prep.).

To compare our measurements of the stellar mass with the literature, it is crucial to estimate the total galaxy stellar mass (M_*) from the aperture stellar mass ($\overline{M}_*$) by applying aperture corrections. These corrections were estimated based on the ratio between the total photometric flux of the galaxy in the *r*-band according to Legacy Survey DR10 (Dey et al. 2019; Zenteno et al. 2025) compared to flux integrated over the same band from each SDSS spectrum (i.e., within the SDSS aperture) and the AGN contribution to the continuum by considering

$$M_* = \overline{M}_* \times \frac{(\text{Total flux}/\text{Aperture flux}) - \mathrm{f_{AGN}}}{1 - f_{\rm AGN}}. \quad (1)$$

The factor multiplying the aperture stellar mass to obtain the aperture corrected stellar mass will be referred to as `aperture correction factor`. By definition, the `aperture correction factor` must be greater than 1, unless the AGN varied significantly between the two observations (photometric and spectroscopic). This is a simplistic aperture correction that assumes the light collected by the fiber is proportional to the galaxy's total light, that there are no significant color gradients within the galaxy, and that the AGN luminosity does not change between observations.

To consider external photometry-based validations, we used three well-documented comparison sets: i) Li et al. (2024) analyzed AGN in eFEDS using the Subaru Hyper Suprime-Cam (HSC), obtaining images in the *grizy* bands, which allowed them to perform a 2D AGN-host image decomposition, in which they removed the nuclear component from the images and used the residual host to compute the physical parameters. ii) Buchner et al. (2024) used available X-ray-to-infrared data in the eFEDS field for the SED-fitting code GRAHSP, which aims to provide unbiased and accurate host galaxy parameters of AGN to specifically address the overestimation issues found in previous methods but consequently yielded larger (and more realistic) error bars. iii) Yu et al. (2023) also used X-ray-to-infrared photometric data in the eFEDS field for SED-fitting, but they employed the widely used code CIGALE, which was updated to treat AGN with more detail than the original version that mainly focused on inactive galaxies. These three methods provide sophisticated approaches for disentangling the host galaxy from the AGN emission using photometry and can serve as a comparison for our spectral method, especially regarding the (aperture-corrected) stellar mass measurements.

The stellar masses of these samples were calculated using the Chabrier initial mass function, whereas we used the Salpeter initial mass function. Therefore, we applied the +0.25 dex correction described by Bernardi et al. (2010). After matching our sources by eFEDS ID, we cleaned the matched samples to avoid problematic cases or changes due to excessive AGN variability by excluding

- $f_{\rm AGN}$ >0.8;
- Redshifts disagreeing with > 0.01 error;
- Unreasonable aperture correction:
  - `aperture correction factor` < 0.5, i.e., fiber flux larger than the total flux by a factor > 2;
  - `aperture correction factor` $> 1.5 \times \left(\frac{20\ \mathrm{kpc}}{2 d_A}\right)^2$, i.e., the aperture correction is larger than required for a galaxy with a 20 kpc radius at the respective redshift, where d_A is the angular distance[1];

[1] The 1.5 scale for this criterion comes from the attempt to conservatively exclude most of the outliers when considering the aperture correction factor with regard to redshift.

- Difference between high and low estimates of the Bayesian distribution of the logarithm of the stellar mass from GRAHSP > 1 (more than one order of magnitude, as in Buchner et al. 2024);
- Flag `above_Mcut` from HSC set to `False`, indicating magnitude saturation;

It is not straightforward to compare the AGN contribution for the different methods because we estimated this parameter within the SDSS aperture, which should yield higher values than when considering the whole galaxy with photometry. After applying the cuts mentioned above, the matching sample with HSC contains 566 objects, the one with GRAHSP contains 734 sources, and the one with CIGALE contains 634 objects.

For the benchmark samples in Sect. 3.1, the redshift range is $z \leq 0.55$ to guarantee that Hα is included in the SDSS wavelength coverage. For the eFEDS sample, however, we have sources at higher redshifts, with $z \leq 1$. We applied the cut at $z = 1$ based on visual inspections (Aydar et al. 2025), since in the SDSS SPIDERS sample, no clear stellar population features (e.g., absorption lines and continuum shape) were visible for $z > 1$ sources.

3.3. Testing against external samples: Stellar velocity dispersion

For the comparison with the stellar velocity dispersion, we considered VLT/X-Shooter and Gemini/GMOS observations of the matching sources from the CL sample (Sect. 3.1), presented in Zeltyn et al. (2026). Of the total 11 matching sources, nine were observed with the X-Shooter 1.6" slit, while the other two were observed with the GMOS 0.5" slit. These observations should provide a larger spectral resolution than the SDSS data.

4. Method validation

In this section we validate our spectral-fitting method by comparing measurements from different observations of the same active galaxies and by comparing spectral-fitting results with SED-fitting and image-decomposition results for the same sources. The analysis of the properties associated with the host galaxy is in Sect. 4.1, and the properties of the AGN in Sect. 4.2. Based on our analysis, we recommend thresholds for measurement reliability. We also address the S/N dependency in our systematic scatters, which show that the suggested quality cuts are sample-dependent and should be reassessed for studies relying on spectra obtained from other instruments and/or with different S/N and redshift distributions.

4.1. Host-galaxy properties

The main optical spectral measurements associated with the stellar populations of the host galaxy used for scaling relations are the stellar mass (M_*) and the stellar velocity dispersion (σ_*). Given the known degeneracies between AGN power-law emission and young stellar populations' emission in the blue part of the optical continuum (e.g., Tadhunter et al. 1996; Holt et al. 2007; Cardoso et al. 2017), the measurement of M_*, which is based on a redder part of the spectra, should be more reliable than the measurement of σ_*, which is based on the absorption lines in a bluer part of the spectra.

4.1.1. Stellar masses

The measurement of the aperture stellar masses ($\overline{M}_*$) is based on the `pPXF` output of the mass-to-light ratio (M/L) from the SSP fitting, to which we associate the flux from the spectra integrated in the DECam-r photometric band coverage (see Appendix B). However, our aperture stellar mass estimates do not necessarily reflect the galaxy's total stellar mass, as at low redshifts, the SDSS fiber may be observing only an inner part of the galaxy. For samples GAL and QSO, since the observations were all from SDSS-V, the comparison should not be affected by aperture effects; instead, differences in $\overline{M}_*$ could indicate effects of the S/N between the different observations and the stacks of the same object, and also provide systematic uncertainties of the fitting results. For the CL sample, however, there is a difference between the observations from SDSS-I and -II 3" fiber and the 2" or 1.3" observations from SDSS-III onward (for APO or LCO, respectively). We emphasize the dependence of $\overline{M}_*$ with redshift and galaxy morphology, so no conclusions regarding the overall stellar mass of the host galaxy should be drawn without providing aperture corrections. However, our internal comparison relies on $\overline{M}_*$ to avoid other sources of uncertainty or systematic biases associated with the aperture correction.

We compared the results for bright and dim states for sample CL and for the `daily` observations with their respective `allepoch` spectrum for samples GAL and QSO. The difference in the measurements for $\overline{M}_*$ is shown in Fig. 5, with the comparison to $f_{\rm AGN}$. The statistical uncertainties obtained from Monte Carlo iterations are very small, ranging from an average of 3% of the stellar mass for sample GAL to 12% for sample QSO, indicating that this is a robust measurement across runs with random noise. The differences among the samples are expected, since measuring stellar properties is more challenging in quasar-dominated spectra. However, when we compare the pairs of observations and calculate the inverse-variance weighted mean and standard deviation (shown in the legend of Fig. 5), we see that the samples have a rather stable ~0.14 dex intrinsic scatter in the stellar mass comparisons, which we take as an estimate of the systematic uncertainty of our stellar mass measurements.

Since high QSO contributions to the continuum can substantially outshine the stellar emission, based on Fig. 5 (and Fig. B.1), we consider only spectra with $f_{\rm AGN} < 0.8$ to have reliable estimates of the properties of the host galaxy, deriving 0.14 dex for the systematic uncertainty of the combination of the samples with $f_{\rm AGN} < 0.8$ ("Clean"). Accounting only for the S/N> 10 observations reduces the scatter to 0.10 dex, showing that the optimal cuts to obtain reliable results depend on a sample's S/N, $f_{\rm AGN}$, and (potentially) redshift distributions. The slight negative inverse-variance weighted mean of the CL sample reflects mostly the difference in the fiber apertures between the SDSS generations, since it indicates that the bright-state measurements yield higher masses than the dim state, and for most of the sources, the bright state was observed with a larger fiber than the dim states (see Fig. 4). Figure 6, which shows a comparison of aperture stellar masses obtained from different observations of the same sources, confirms that sources with $f_{\rm AGN} > 0.8$ — shown with large markers — are among those that deviate mostly from the 1:1 relation.

Regarding the test against external samples, Fig. 7 shows the comparison of the stellar masses from the eFEDS field from our method (`pPXF`) with the results from Li et al. (2024, HSC), Buchner et al. (2024, GRAHSP), and Yu et al. (2023, CIGALE). We found systematic offsets of 0.19, -0.06, and 0.05 dex for HSC, GRAHSP, and CIGALE, respectively, which are significantly

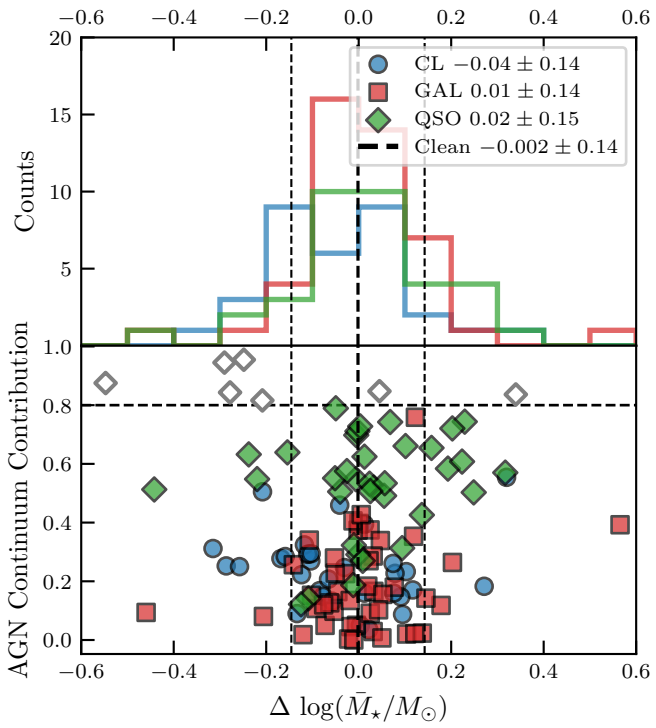

Fig. 5. Difference of the aperture stellar masses as a histogram for the different samples on the top and against the fraction of the AGN contribution to the continuum ($f_{\rm AGN}$) at the bottom. For sample CL (blue), the symbols indicate $\log(\overline{M}_*/M_\odot)_{\rm dim} - \log(\overline{M}_*/M_\odot)_{\rm bright}$, while for samples GAL and QSO (red and green, respectively) we display $\log(\overline{M}_*/M_\odot)_{\rm allepoch} - \log(\overline{M}_*/M_\odot)_{\rm daily}$. The $f_{\rm AGN}$ values shown correspond to the bright-state spectra for the CL sample and to the `daily` spectra for the GAL and QSO samples. The inverse-variance-weighted mean and standard deviation for each sample are shown in the legend. The lower panel shows a horizontal dashed line at $f_{\rm AGN} = 0.8$, which can be used as a threshold to exclude spectra whose $\overline{M}_*$ difference is more significant, indicating less reliable measurements. The "Clean" sample considers all spectra from samples CL, GAL, and QSO with $f_{\rm AGN} < 0.8$; we indicate its mean and standard deviation with the vertical dashed lines in both panels.

smaller than the dispersion (0.31, 0.41, and 0.35 dex for HSC, GRAHSP, and CIGALE, respectively). Our results are therefore somewhat intermediate between these methods. In fact, the comparison between HSC and GRAHSP, regardless of our method, yields a scatter of 0.29 dex, while the comparison of CIGALE with both HSC and GRAHSP separately yields 0.31 dex of scatter; these scatters are all comparable to that between our method and HSC. Hence, we conclude that a systematic scatter of 0.3-0.4 dex between our results and the literature is within expectations and validates our methodology as competitive with some of the most refined photometric techniques available for dealing with AGN with significant host-galaxy emission. These results also demonstrate that our "internal" systematic uncertainties of 0.14 dex from Fig. 5 are smaller than those from comparisons with other observations of the same objects.

4.1.2. Velocity dispersion

Figure 8 displays the comparison of the estimates for the stellar velocity dispersion (σ_*). Following the recommendations for velocity dispersion measurements obtained from BHM optical spectra due to the finite resolution of the instrument[2], we excluded the measurements of $\sigma_* < 70$ km s^{-1} from the histograms in the top panel of Fig. 8. They are shown in gray in the bottom panel, and excluding such cases in which the measurement is below the instrumental resolution of SDSS data eliminates some, but not all, of the most discrepant cases between two measurements of the same source. Both GAL and QSO samples have outliers with $\sigma_* > 70$ km s^{-1} and an absolute difference between spectra of > 100 km s^{-1}, which makes the scatter larger than the sample CL. For the CL sample, the positive offset indicates that most dim measurements have a higher σ_* than in the bright state, as expected, since in the bright state the host galaxy absorption lines (which are key to constrain σ_*) are diluted by the stronger AGN contribution. We also show in gray the cases with $f_{\rm AGN} > 0.8$, which are not considered for the histograms. The overall standard deviation for the difference in velocity dispersion, considering all samples and excluding $\sigma_* < 70$ km s^{-1}, is 35 km s^{-1}, and it improves to 27.5 km s^{-1} when we consider only observations with S/N > 10. In Fig. 9, we compare the measured velocity dispersions across the various observations for the CL, GAL, and QSO samples. Dotted lines are the limits of the instrumental resolution $\sigma_* = 70$ km s^{-1}, and we highlight in gray shaded areas the dispersion of 35 km s^{-1} above such a threshold, for cases that should be considered with caution. The spectra with $f_{\rm AGN} > 0.8$, shown with larger markers, lie mainly within caution or non-reliability regions and exhibit large error bars.

Regarding the comparison of the 11 CL objects observed with SDSS and either X-Shooter or GMOS (Zeltyn et al. 2026), we obtain a scatter of 34 km s^{-1}, which confirms our systematic uncertainty of 35 km s^{-1}, despite the different slit sizes (1.3", 2", or 3" for SDSS, against 1.6" for X-Shooter and 0.5" for GMOS). It is worth noting that GMOS and X-Shooter should provide higher spectral resolution, yielding more precise velocity dispersion measurements, but since all measurements matching our sources exceed the SDSS instrumental limit of 70 km s^{-1}, this should not significantly affect the comparison. We also note that, in our comparisons, the absolute difference between the SDSS and GMOS or X-Shooter observations is always below 70 km s^{-1}, demonstrating the efficiency of our method, as it falls within the SDSS spectral resolution limits.

Concluding this section, based on the reported set of internal and external validation tests, we recommend trusting the measurements of properties from the stellar populations when the AGN contribution to the continuum is $f_{\rm AGN} < 80\%$. For the stellar masses, we recommend using a systematic uncertainty of 0.14 dex. In the case of the stellar velocity dispersion, SDSS BOSS observations with measurements of $\sigma_* < 70$ km s^{-1} are unreliable, and those with $70 \leq \sigma_* < 105$ km s^{-1} should be considered with caution. Therefore, we recommend using the Monte Carlo statistical uncertainties for each σ_* measurement, keeping in mind the SDSS limit and the systematic uncertainty obtained in this work. If one is interested in measuring $\sigma_* < 70$ km s^{-1}, data with higher spectral resolution than SDSS should be preferred.

4.2. AGN properties: Black hole mass

The main property to describe SMBHs is their mass. There are different methods to estimate the mass of an SMBH, and in this section, we focus on the single-epoch virial estimates (e.g., Vestergaard & Peterson 2006; Shen et al. 2011, 2024). A discussion on the validity of such an approach for a sample of changing-look AGN (sample CL) is presented in Sect. 5.2. The

[2] https://www.sdss.org/dr18/bhm/caveats/

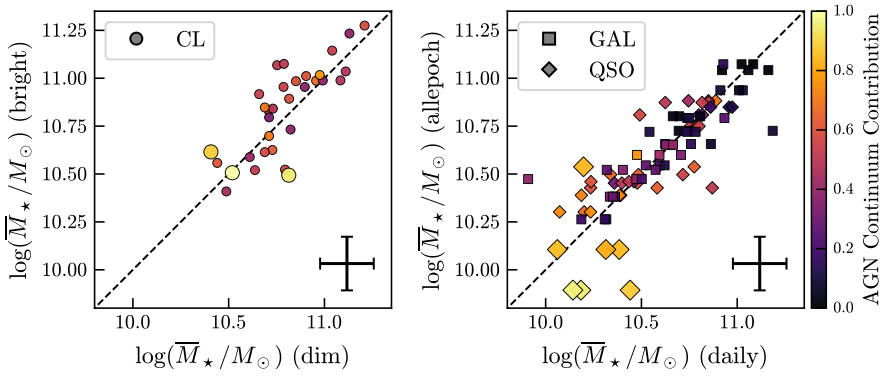

Fig. 6. Comparison of aperture stellar masses between different observations of the same sources. The diagonal lines indicate the 1:1 relation. The left panel shows a comparison of the bright and dim states of the sample CL (circles), color coded by the AGN contribution to the continuum ($f_{\rm AGN}$) in the bright spectra. The right panel presents the comparison fits of individual spectra (`daily`) to stacked spectra (`allepoch`) for samples GAL (squares) and QSO (diamonds); color coded according to the $f_{\rm AGN}$ of each `daily` observation. The larger markers indicate $f_{\rm AGN} > 0.8$; their measurements of host-galaxy properties are less reliable. The black crosses indicate the systematic uncertainty derived from Fig. 5.

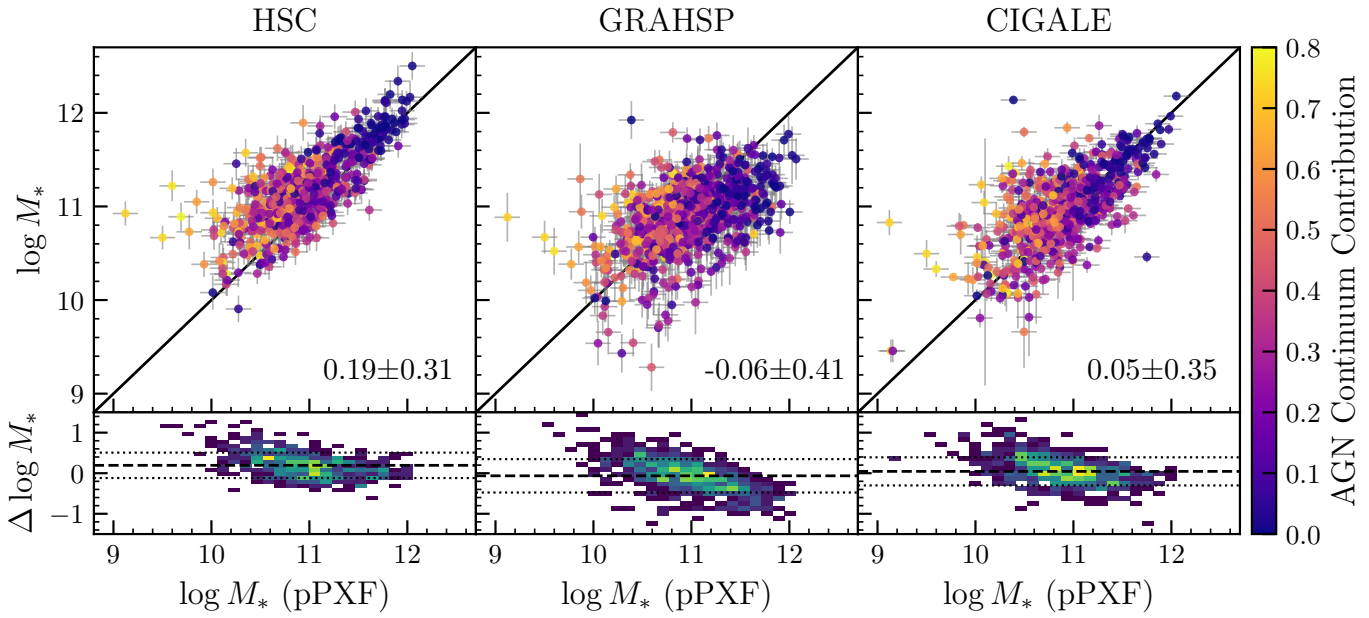

Fig. 7. Comparison of (aperture-corrected) stellar masses obtained from our spectral-fitting method (`pPXF`) with an image decomposition method (HSC on the left, Li et al. 2024) and two SED-fitting methods (GRAHSP in the center, Buchner et al. 2024; and CIGALE on the right, Yu et al. 2023). In the top panels, the data are color coded by $f_{\rm AGN}$, and the 1:1 relation is shown as a black line. The bottom panels show the density distribution of the ratio of stellar mass measurements, with the dashed line indicating the offset and the dotted lines indicating the scatter. The mean offset and the scatter (in dex) are displayed in the bottom-right corner of each upper plot.

single-epoch method depends on reliably measuring the width (and in some cases the luminosity) of broad lines. Therefore, to guarantee a reliable detection of a broad component in the emission-line fitting, we used the following criteria:

$$\begin{aligned} &\mathrm{FWHM_{broad}}/\mathrm{FWHM_{broad\_error}} > 3, \\ &\mathrm{Flux_{broad}}/\mathrm{Flux_{broad\_error}} > 3. \end{aligned} \quad (2)$$

Given the redshift range of our sample, we focused on the SMBH mass estimates from Hα and Hβ. Assuming the virial factor $\langle f \rangle = 0.68 \pm 0.15$ (Batiste et al. 2017), the Hα SMBH mass estimate is given by Dalla Bontà et al. (2025) as

$$\begin{aligned} \log\left(\frac{\mathrm{M_{BH,H\alpha}}}{\mathrm{M_\odot}}\right) = 0.81 \log\left(\frac{\mathrm{L_{H\alpha,BR}}}{10^{42}\mathrm{L_\odot}}\right) + \\ + 1.63 \log\left(\frac{\mathrm{FWHM}}{10^{3.5}\mathrm{km\ s^{-1}}}\right) + 7.37, \end{aligned} \quad (3)$$

while for Hβ from Shen et al. (2024) we adopted

$$\log\left(\frac{\mathrm{M_{BH,H\beta}}}{\mathrm{M_\odot}}\right) = 0.5 \log\left(\frac{\mathrm{L_{5100}}}{10^{44}\mathrm{L_\odot}}\right) + 2.0 \log\left(\frac{\mathrm{FWHM}}{\mathrm{km\ s^{-1}}}\right) + 0.85, \quad (4)$$

where $\mathrm{L_{H\alpha,BR}}$ is the luminosity measured from the broad-component of Hα, FWHM is measured from the broad component of the emission line in both cases, and $\mathrm{L_{5100}}$ is the AGN continuum luminosity at 5100 Å. Figure 10 provides the relation between the AGN continuum and the broad-line luminosities that are assumed for applying the single-epoch method, according to Dalla Bontà et al. (2025) and Eq. 3. We also display the total luminosity at 5100 Å, showing that our decomposition method can shift the objects toward the expected relation when we consider only the AGN contribution to the continuum. Many of the sources for which the conditions of Eq. 2 do not apply are outliers in sample GAL, which is a sample of mostly narrow-line AGN. However, through visual inspection, we find cases in which the

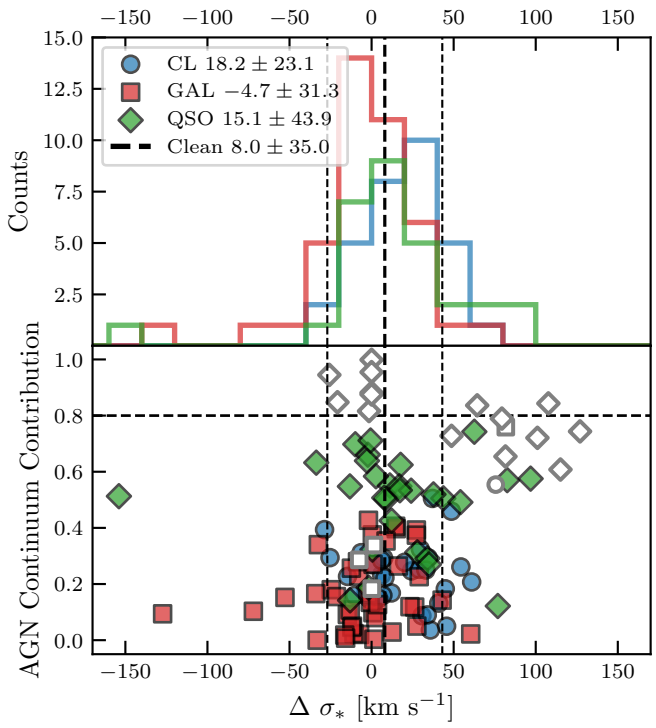

Fig. 8. Difference of the stellar velocity dispersion displayed as in Fig. 5. Given the instrumental resolution of SDSS, only measurements with $\sigma_* > 70$ km s^{-1} are included in the histogram and statistics. The pairs of spectra with `daily` $f_{\rm AGN} > 0.8$ or for which at least one of the spectra has $\sigma_* < 70$ km s^{-1} are indicated in gray in the bottom panel.

GAL observation that lies as an outlier (i.e., more than 3σ from the luminosity relation from Dalla Bontà et al. 2025) shows examples of AGN with a significant host-galaxy emission and also a significant broad Hα component, despite the narrow line being more prominent than the broad component. These objects are not usually considered for calibrating single-epoch black hole mass estimates, and though our code allows one to measure the properties of their (faint) broad emission lines, these measurements should be considered with caution.

Figure 11 shows the comparison of the results for the SMBH mass from Eq. 3. Different from Sect. 4.1, we show the difference for bright−dim results for sample CL, since the bright spectra should be the most reliable for AGN measurements. As seen from the gray markers in the bottom panel of Fig. 11 and expected from the sample selection, 51% of the sample GAL showed the absence of a significant broad component in the Hα emission line, although all samples have such cases of nonreliable broad-line measurement (16% for sample CL and 29% for sample QSO). The largest standard deviation is from the CL sample, 0.24 dex, as expected since the BLRs of CL-AGN are not necessarily virialized (a more detailed analysis of the effects on the FWHM and on the line luminosity for the "breathing" of the BLR is given in Sect. 5.2). Therefore, we consider only the QSO and GAL samples for the statistics of the "Clean" sample, since these should be virialized systems for which the single-epoch mass estimate can be reliably applied, yielding a 0.1 dex scatter.

The scatter obtained in our sample is in addition to the systematic scatter associated with using the single-epoch mass estimate for large samples of black holes, estimated to be 0.3 – 0.5 dex (e.g., Shen 2013). We expected our scatter to be smaller than the systematic uncertainty of the virial black hole mass estimate since the geometry of the systems in samples GAL and QSO should not change significantly between the observations, as seen from their scatter of 0.10 dex in Fig. 11. Indeed, as seen in Fig. 12, by considering the quality cuts of Eq. 2, samples GAL and QSO are within the expected systematic scatter of the method, shown as gray areas. For sample CL, there is a strong trend in estimating higher black hole masses for the bright sources, which could indicate that the continuum and the line width are not behaving as expected for a "breathing" BLR (see more in Sect. 5.2). We believe this trend in sample CL is more closely related to sample selection than to the fitting method, as indicated by the agreement for the GAL and QSO samples.

Regarding the SMBH mass estimates from Hβ, Fig. 13 shows the comparison of the measurements in a similar fashion to Fig. 11. Sample GAL contains very few cases with a significant broad Hβ component, and since sample CL was constructed based on the spectra having broad Hα but often with the dimming/brightening based on the disappearance/appearance of a broad component of Hβ, many cases did not show a trustworthy Hβ component according to Eq. 2. The objects without a significant broad Hβ line correspond to 72% of the sample CL, 84% of the sample GAL, and 22% of the QSO sample. For both Hα and Hβ, the bright CL spectra tend to have higher SMBH mass estimates in comparison to the dim state. However, by construction, both samples CL and GAL have too few sources with a pair of reliable broad lines for a trustworthy statistical scatter, whereas sample QSO was built based on broad-line detections from the SDSS pipeline classification. Hence, the selection effects on the construction of the samples are playing a larger role than a general assumption of the validity of Eq. 3 in comparison to Eq. 4. Nevertheless, the 0.13 dex scatter of the "Clean" sample of reliable broad Hβ measurements for the GAL and QSO samples is consistent with the results for Hα, though it is slightly larger and based on fewer data points. Figure 14 shows that overall, the couples of Hβ-based mass measurements scatter further from the 1:1 line, with most within the 0.5 dex expected for single-epoch mass measurements. The objects beyond the scatter are from the CL sample and have larger systematic uncertainties, as in Fig. 12. Since the continuum luminosity is used instead of the line luminosity in Eq. 4, the black hole mass estimates with Hβ rely more on a correct AGN continuum estimate than Hα, and therefore the slightly larger scatter seen in Fig. 13 for the QSO sample could be due to these measurements being more sensitive to the host-galaxy decomposition.

We examined the effect of different S/N ranges on AGN properties, considering only the GAL and QSO samples with reliable broad-line measurements. For the black hole masses estimated from Hα, there is no significant change when considering observations with S/N> 5, and the scatter improves slightly (from 0.10 to 0.09 dex) when accounting for S/N> 10. For measurements based on Hβ, the influence of the S/N cuts is more evident but still mild, with the scatter of S/N> 10 observations being 0.08 dex, though we are dealing with fewer sources in general. Hence, it is important to consider how data quality influences the reliability of the obtained results.

Finally, Fig. 15 shows the SMBH mass estimate from single-epoch estimates, comparing the measurements from Hα and from Hβ for the spectra that have reliable broad components of both lines simultaneously. Most of the results fall within the expected systematic uncertainty, indicating that the measurements of the FWHM of the broad component and the luminosity are adequate. However, there are many cases beyond the expected 0.5 dex scatter, which may be due to residual cross-calibration uncertainties from Eqs. 3 and 4, which use different reference samples. In

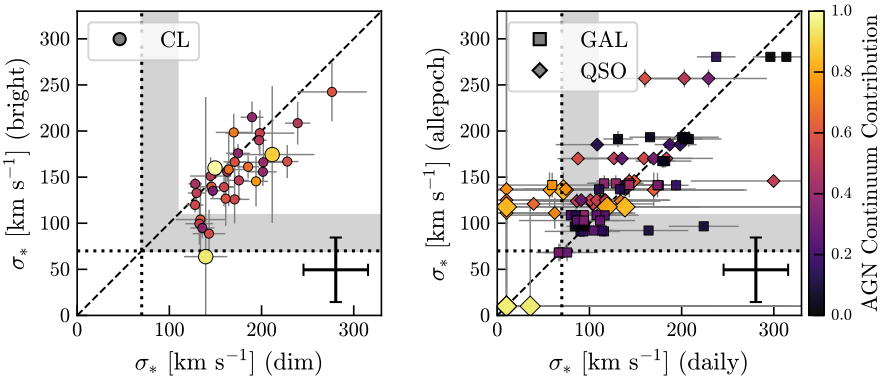

Fig. 9. Comparison of stellar velocity dispersions, similar to Fig. 6. The dotted lines indicate the limits of the instrumental resolution of SDSS (70 km s^{-1}). The shaded regions indicate the 35 km s^{-1} scatter from Fig. 8. Results with $\sigma_* < 70$ km s^{-1} should not be trusted, and the shaded area indicates cases that should be treated with caution.

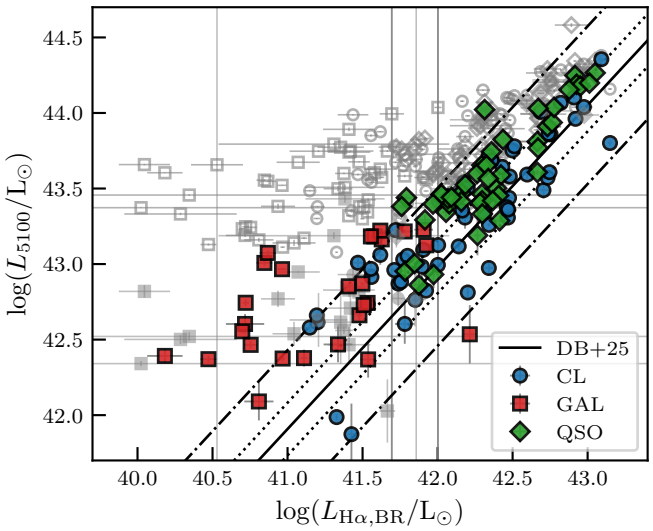

Fig. 10. Relation between the AGN continuum luminosity and the broad Hα luminosity required to apply the single-epoch method as in Dalla Bontà et al. (2025) or Eq. 3 (diagonal line, with one sigma in dotted lines and three sigma in dotted-dashed lines). The empty gray markers indicate the total luminosity at 5100 Å before the decomposition into AGN and host-galaxy contributions. The filled gray markers indicate the sources that do not pass the criteria of Eq. 2.

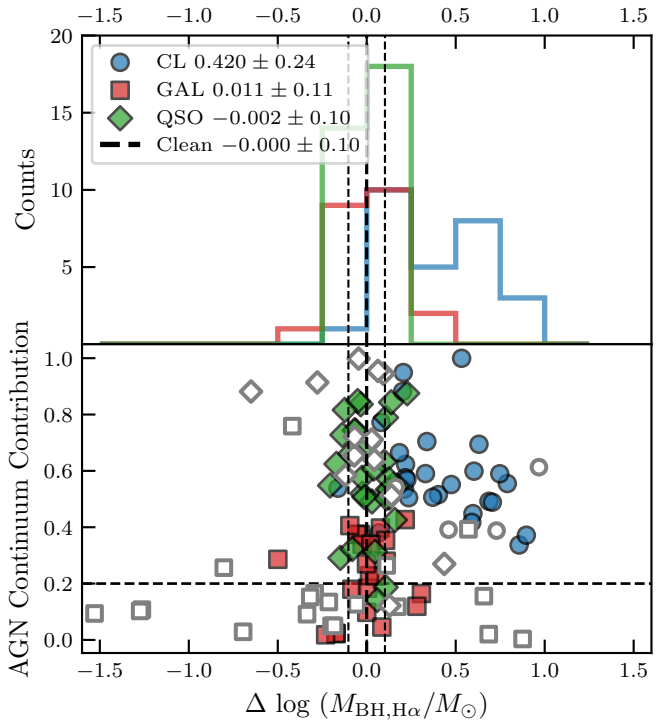

Fig. 11. Difference of single-epoch estimates of the SMBH mass from Hα. This is similar to Fig. 5, but compares $\log(M_{BH,H\alpha}/M_\odot)_{bright} - \log(M_{BH,H\alpha}/M_\odot)_{dim}$. The f_{AGN} is from the dim state for the sample CL. The gray markers in the bottom panel indicate the cases in which the measurement of a broad component for the fit of Hα was not reliable according to Eq. 2. The "Clean" sample statistics do not include these sources nor the CL sample since changing-look AGN might not be virialized systems (see Sect. 5.2).

this respect, we note here that the sample selection of this work did not allow for a systematic evaluation of single-epoch SMBH mass estimates for the Hα and Hβ in the sense of attesting which is more reliable since sample CL is biased for showing broad Hα without a broad Hβ component and sample GAL is biased for not having significant broad emission lines. Future work will include applying this method to larger, less biased samples, enabling the assessment of the quality of single-epoch estimates.

5. Further results and discussion

5.1. Scaling relations

The investigation of whether SMBH growth is coupled to the host-galaxy evolution is supported by empirical scaling relations, in which the mass of the SMBH is related to the stellar velocity dispersion and the stellar mass of the bulge or the host galaxy (e.g., Gebhardt et al. 2000; Tremaine et al. 2002; Kormendy & Ho 2013; Suh et al. 2020). Once such properties are measured for our sample, we can check if the results match the expected low-redshift scaling relations. Since we are dealing directly with the spectral data, we do not distinguish between galaxy substructures, such as the bulge, and we also do not differentiate our sources based on the morphological classification of the host galaxies. However, the aim of this discussion is not to make a general statement about the position of AGN in the scaling-relation planes, since our sample is biased in its selection (e.g., Lauer et al. 2007; Li et al. 2025); in future work, we will use our decomposition in less biased samples to draw conclusions about the co-evolution of AGN and their host galaxies (Aydar et al., in prep.).

We show the results for the aperture-corrected stellar mass (M_*) in comparison to the SMBH mass in Fig. 16, with the scaling relations from Reines & Volonteri (2015), Suh et al. (2020), and

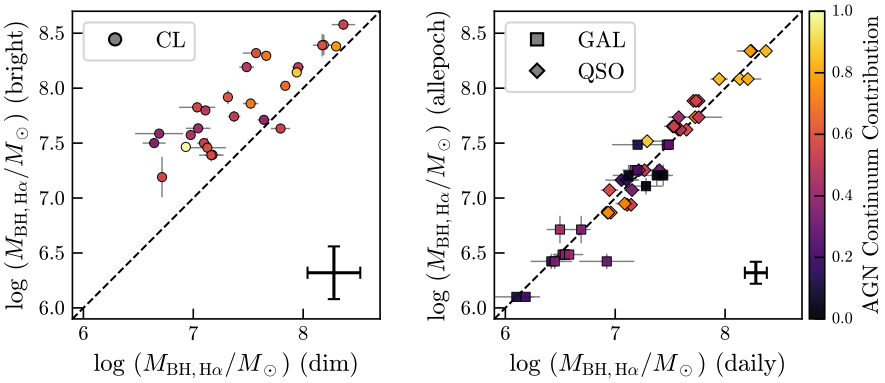

Fig. 12. Comparison of SMBH mass according to single-epoch estimates using Hα, similar to Figure 6. The gray band represents the systematic 0.5 dex uncertainty inherent in single-epoch black hole mass estimates (Shen 2013). The systematic uncertainty shown in the left panel is the 0.24 scatter for the CL sample, while the one in the right panel is the 0.10 scatter for the "Clean" sample, according to Fig. 11.

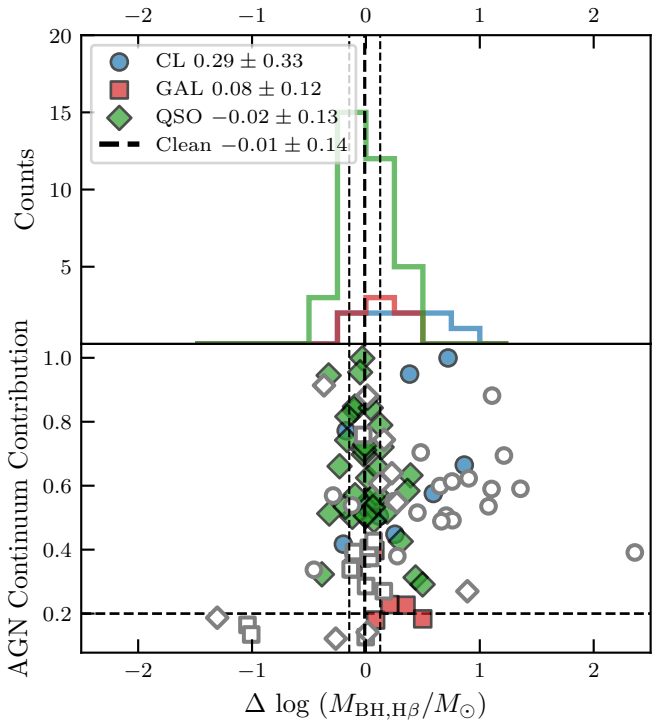

Fig. 13. Difference of the SMBH mass according to single-epoch estimates using Hβ, displayed as in Fig. 11.

Pucha et al. (2025). For the CL sample, we show in gray the results for $\overline{M}_*$ (i.e., before aperture correction) because this sample was selected due to the variability of the sources, and therefore the flux from Legacy Survey DR10 cannot be representative of both the dim and the bright states, adding an irreducible uncertainty to the extent of such corrections. The samples CL dim and GAL show fewer objects, as they often do not exhibit a significant broad Balmer line, especially for Hβ (see Figs. 11 to 14). For the M_{BH}-σ_* relation shown in Fig. 17, our data are in broad agreement with the scaling relation proposed by Kormendy & Ho (2013).

Overall, the general agreement between our results and the expectations of the scaling relations demonstrates the success of our method in extracting simultaneous information about the AGN and the stellar population from a single spectrum. This result further indicates that our decomposition method produces reliable information for studying the co-evolution of SMBHs and their host galaxies when applied to larger, less biased samples.

5.2. Broad-line region "Breathing"

Although our methodology is validated by its ability to measure consistent conserved parameters, not all spectral features across different observations are expected to be the same. For example, while the SMBH mass should be constant, the FWHM of the broad line and the luminosity that are used in the equation for the single-epoch mass derivation are not expected to be the same in different epochs, although they are expected to vary accordingly assuming photoionization equilibrium in a virialized system (e.g., Park et al. 2012; Barth et al. 2015). This effect of the correlation between the BLR and the AGN luminosity has been analyzed in reverberation mapping studies, which are the basis for the proposal of single-epoch mass estimates, and it is referred to as the BLR "breathing" (e.g., Runco et al. 2016). Physically, it means that for a virialized system in photoionization equilibrium, as the AGN luminosity increases, the average BLR size should increase, and therefore the average broad-line width should decrease (Wang et al. 2020).

The analysis of the breathing properties on broad Hα lines in our samples is shown in Figure 18. This figure compares the different estimates of FWHM and the luminosity of the broad Hα component (fitted with a combination of three Gaussians) according to Eq. 3 for each pair of observations[3]. The lines indicate the expected slope (α = Δlog FWHM/Δlog L) if the BLR was breathing according to Eq. 3 (dashed) and the relation proposed empirically for the Hα breathing by Wang et al. (2020) (dot-dashed). We do not include sample GAL, since these objects are, by definition, not broad-line galaxies, and when a broad-line component is detected, it is not dominant compared to the narrow component of the emission line.

From the diagram, we see that sample QSO is more concentrated in the locus of very small differences between the observations, indicated by the dotted lines at zero in both axes. This distribution demonstrates that our methodology is robust, as the sample construction should not result in significant differences across observations. However, sample CL, also by construction, has larger differences in both width and luminosity. The objects that showed a significant deviation from the "Clean" scatter in Fig. 11 are shown in purple and were already candidates for non-virialized systems; this hypothesis is further strengthened by their distribution farther from the expected behavior of a breathing virialized BLR. The cumulative distributions of the slope α shown in the right panel of Fig. 18 also reinforce that hypothesis. The mean slope of the overall CL sample (-0.09) lies closer to the empirical expectations for a breathing BLR of -0.06 according

[3] The results for Hβ are not displayed due to the lower number of sources with a reliable broad component according to Eq. 2.

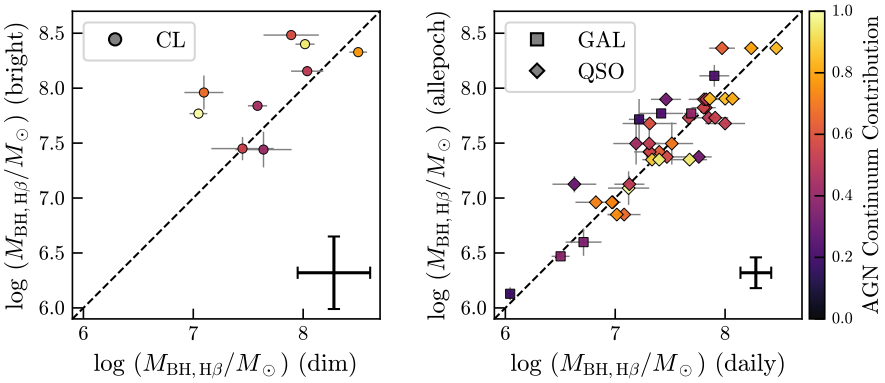

Fig. 14. Comparison of SMBH mass according to single-epoch estimates using Hβ, displayed as in Figure 12. The systematic uncertainties are shown in the bottom right of the plots, with 0.33 for the CL sample and 0.14 for the GAL and QSO samples, as in Fig. 13.

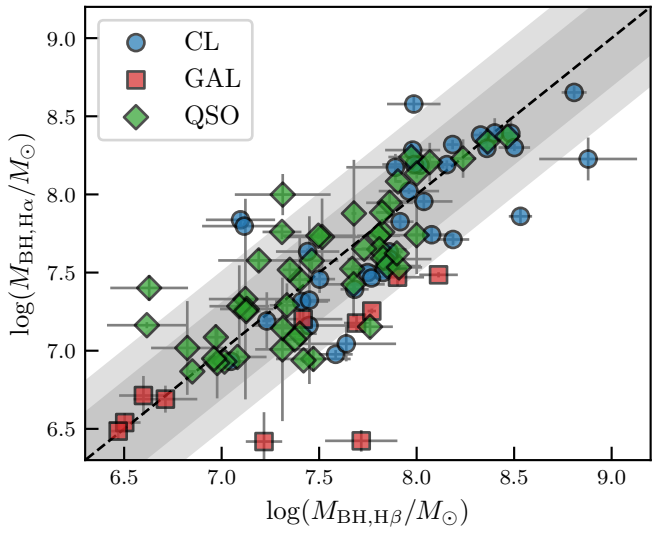

Fig. 15. Comparison of SMBH mass single-epoch estimates using Hα and Hβ for each source in which both broad lines are in agreement with Eq. 2. The gray-shaded areas around the 1:1 relation indicate systematic scatter of 0.3 and 0.5 dex, as reported by Shen (2013).

to Wang et al. 2020; however, after excluding the outliers (purple points), the mean of the slope (-0.17) is in better agreement with the -0.2 model (according to Eq. 3) expectations, showing the importance of reliable cleaning procedures before stating the validity of one or another approach. It would be interesting to further test this analysis in larger samples (e.g., Zeltyn et al. 2024) to verify if such outliers are indeed non-virialized changing-look AGN, probably due to the appearance or disappearance of a BLR caught in the act by the CL selection (Ricci & Trakhtenbrot 2023).

On the top and left axes of the left-hand panel from Fig. 18 we show the contribution of each parameter to the estimate of the SMBH mass according to Eq. 3. The differences in the FWHM are more significant to the overall scatter of the SMBH masses than the luminosity. Hence, this result shows that most of the uncertainty in the SMBH mass estimates in this work is intrinsically associated with the BLR breathing behavior rather than with limitations of the decomposition method. A more general discussion on the limitations of the single-epoch SMBH mass estimates is beyond the scope of this paper and can be found in, for example, Shen (2013) and Shen et al. (2024).

6. Conclusions and outlook

In this work, we developed validation tests for high-quality automatic spectral fitting of galaxy-AGN hybrid spectra. We presented benchmark data samples used to validate stellar mass, stellar velocity dispersion, and SMBH mass estimates from Hα and Hβ over a range of signal-to-noise ratios and AGN-to-galaxy contrast ratios. The "internal" benchmark samples consisted of objects observed multiple times by SDSS: 32 changing-look AGN and 30 eROSITA sources, among which 15 are classified as "QSO" and 15 as "GALAXY" by the SDSS pipeline (Sect. 3). The tests were applied to a two-step spectral-fitting method based on `pPXF` (Sect. 2.1) and `PyQSOFit` (Sect. 2.2), where galaxy contamination is subtracted before fitting the AGN emission. The methodology was successful and can provide reliable measurements of emission and absorption line properties as well as the AGN continuum (Sect. 4).

We have also provided "external" comparisons with literature samples to validate the stellar mass estimates by comparing photometric data to SDSS spectra from the eFEDS field and to validate the stellar velocity dispersion by using Gemini and VLT observations of some CL-AGN from our benchmark sample. All comparisons yielded consistent results that validate our methodology and derived uncertainties.

Our methodology is more complex than using SDSS pipeline information (which does not differentiate the broad and narrow components of emission lines), than using `pPXF` alone (which does not have a complex fitting for the AGN contribution for both the line shapes and the continuum), and than using `PyQSOFit` alone (which does not properly account for the host-galaxy contribution). As a corollary, this approach permits one to place a galaxy in scaling relations based on stellar and broad-line properties using the same observation, provided it exhibits significant emission from both the stellar populations and the BLR. Despite being tested on the parameters associated with the scaling relations, our method also provides measurements of the emission lines (overall, narrow, and broad components), AGN continuum, SSPs, and absorption lines, which can provide the estimate of many other physical properties and the selection of subsamples based on, for example, AGN classification, the presence of specific lines such as coronal lines, and the presence of outflows. Although the approach was tailored for fitting SDSS data, it can be generalized and applied to any optical spectrum, making this a powerful tool for future large surveys, such as DESI, 4MOST, and PFS.

Based on our work, we advise relying on the results associated with the decomposed host galaxy if $f_{\rm AGN} < 80\%$, where $f_{\rm AGN}$ corresponds to the fraction of the AGN contribution to the continuum (power law featureless continuum, Fe II pseudo-continuum,

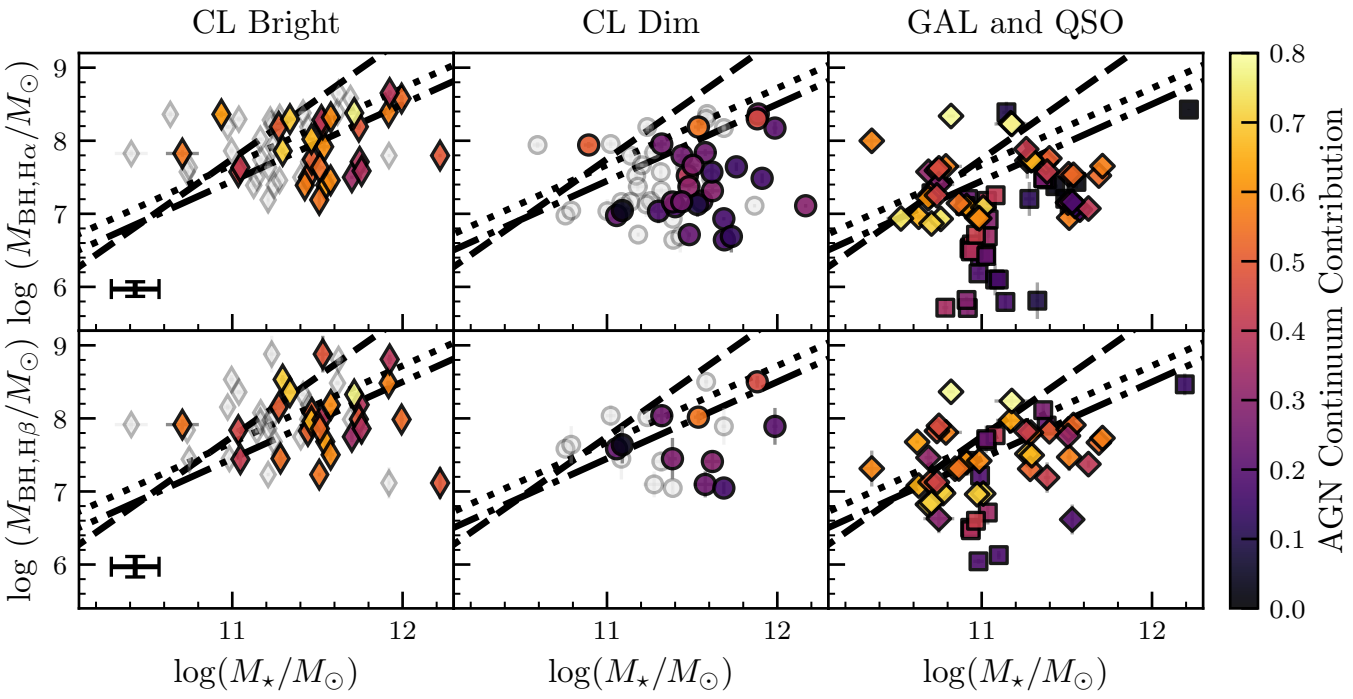

Fig. 16. Scaling relation between the mass of the SMBH and the stellar mass, color coded by the AGN contribution to the continuum in comparison to the host-galaxy emission. Upper panels show the estimates of the SMBH from Hα, while bottom panels display the estimates from Hβ. Left panels present the results for the CL bright spectra in diamonds, middle panels show the results for the CL dim spectra in circles, and the right panels present samples GAL and QSO in squares and diamonds, respectively. We excluded the cases with $f_{AGN} > 0.8$ since their host-galaxy properties are less reliable. We also only considered the cases with a reliable single-epoch SMBH mass estimate according to Eq. 2. For the CL sample in the left and middle panels, for which the aperture corrections are more uncertain, we display the aperture stellar masses (i.e., before aperture correction, $\overline{M}_*$) in gray, equivalent to lower limits of the galaxy stellar mass. The lines indicate scaling relations according to the literature, with the dot-dashed lines representing Reines & Volonteri (2015), the dashed lines representing Suh et al. (2020), and the dotted lines representing Pucha et al. (2025). The statistical uncertainties from Monte Carlo runs are plotted alongside the color coded markers, but are often too small to be seen; we also plot the systematic uncertainty for reference on the reliability of the data.

and Balmer high-order and continuum emission) in comparison to the stellar population (SSPs), calculated from the weight of the templates over the whole wavelength range for each spectrum. Otherwise, the measurements will be biased by the known degeneracy between the featureless power-law continuum emission from the AGN and the young and blue stellar populations (Sect. 4.1). For AGN measurements, we advise using the line-quality criteria from Eq. 2 to obtain reliable measurements (Sect. 4.2). However, since we also noticed an S/N dependence that often, but not always, yields smaller scatter in the comparisons of different observations of the same objects, we advise each user of our methodology to also check on how the S/N, f_{AGN}, and redshift affect their data to then tailor the best quality cuts.

The stellar masses are consistent with internal and external comparisons after aperture corrections based on photometric observations from other surveys, although these corrections are only rough approximations for CL-AGN due to their expected flux changes. We found an "internal" systematic uncertainty of 0.14 dex, which is significantly smaller than the scatter in the comparison with the most robust photometric-based methods for stellar mass estimation (0.3-0.4 dex). Stellar velocity dispersion measurements should only be considered above the instrumental resolution (70 km s^{-1} for SDSS) and should be taken with caution if $\sigma_* < 105$ km s^{-1} by applying our method to SDSS data regardless of the S/N of the observation.

The SMBH mass estimates obtained via the single-epoch method incur an additional systematic uncertainty of ~ 0.1 dex for Hα and Hβ. This is smaller than the systematic scatter of $0.3 - 0.5$ dex currently inherent in large samples of virialized systems from single-epoch measurements. Since we were comparing multiple observations of the same objects rather than analyzing the scatter of a large diverse sample, this result confirms the accuracy of our method.

The results of our technique applied to the testing samples indicate that our selection of AGN is broadly consistent with the literature scaling relations, which correlate the SMBH mass with the stellar velocity dispersion and the stellar mass of the host galaxy (Sect. 5.1). When applied to the CL-AGN, the results show some interesting deviations from the expectation of "breathing" virialized BLRs for a subset of sources, which exhibit higher discrepancies in black hole mass estimates and are candidates for non-virialized systems (Sect. 5.2).

In conclusion, we have demonstrated that our method of applying `pPXF` and `PyQSOFit` for fitting AGN with a significant host-galaxy contribution is robust, and given the uncertainties, it can provide consistent results for the black hole and host-galaxy properties that should not change drastically in short periods of time. This methodology can be applied to other optical spectral samples and thereby improve our understanding of the co-evolution of SMBHs and their host galaxies. In the future, we intend to apply this method to the overall SPIDERS sample within the BHM collaboration between SDSS-V and eROSITA (see Aydar et al. 2025; Kollmeier et al. 2026). From this sample of 200k X-ray-selected AGN with optical spectra, we estimate that

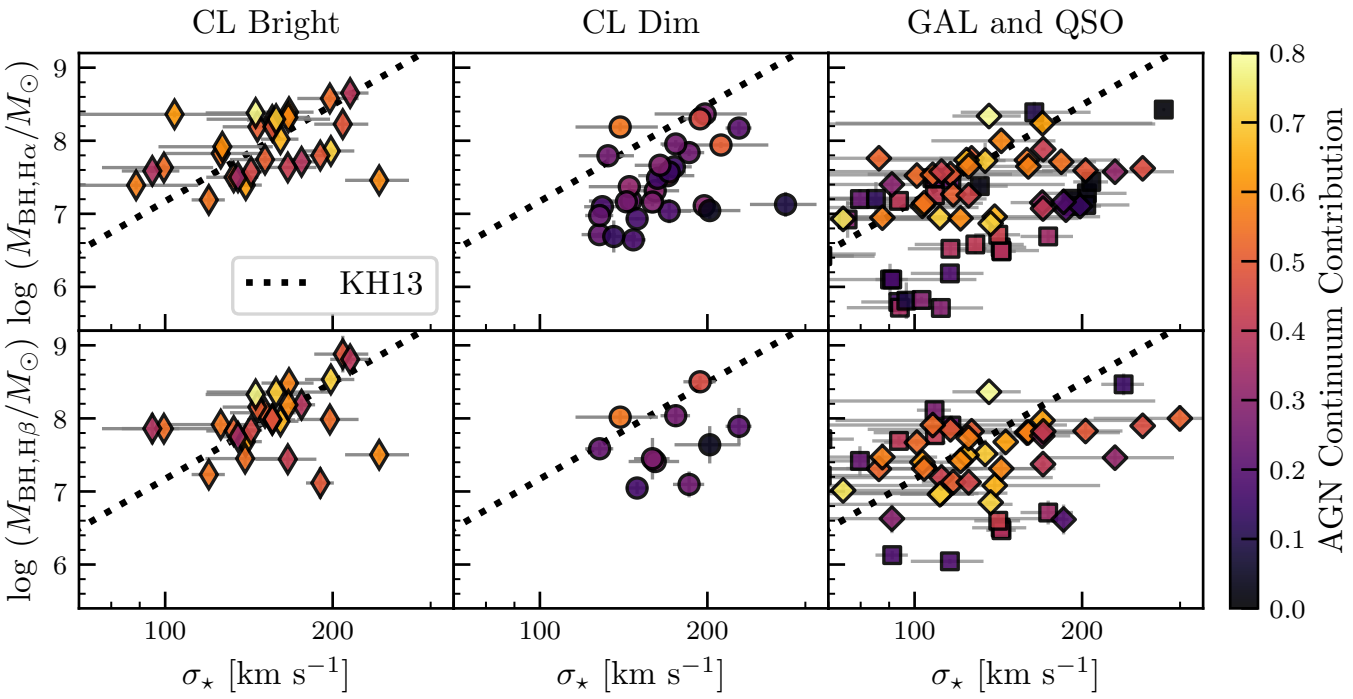

Fig. 17. Scaling relation between the mass of the SMBH and the stellar velocity dispersion, similar to Fig. 16. The dotted line indicates the scaling relation, as described by Kormendy & Ho (2013).

~ 30% of the sample (~ 60k spectra) should require a proper decomposition of the host galaxy and the AGN. The `python` script of this method will be made available on the SDSS `GitHub`[4] together with the 20th Data Release and the Value Added Catalog containing measurements of the emission lines, continuum, and (when detected) absorption lines and stellar population properties of the SPIDERS sample.

Acknowledgements. Funding for the Sloan Digital Sky Survey V has been provided by the Alfred P. Sloan Foundation, the Heising-Simons Foundation, the National Science Foundation, and the Participating Institutions. SDSS acknowledges support and resources from the Center for High-Performance Computing at the University of Utah. The SDSS website is www.sdss.org. SDSS is managed by the Astrophysical Research Consortium for the Participating Institutions of the SDSS Collaboration, including the Carnegie Institution for Science, Chilean National Time Allocation Committee (CNTAC) ratified researchers, Caltech, the Gotham Participation Group, Harvard University, Heidelberg University, The Flatiron Institute, The Johns Hopkins University, L'Ecole polytechnique fédérale de Lausanne (EPFL), Leibniz-Institut für Astrophysik Potsdam (AIP), Max-Planck-Institut für Astronomie (MPIA Heidelberg), Max-Planck-Institut für Extraterrestrische Physik (MPE), Nanjing University, National Astronomical Observatories of China (NAOC), New Mexico State University, The Ohio State University, Pennsylvania State University, Smithsonian Astrophysical Observatory, Space Telescope Science Institute (STScI), the Stellar Astrophysics Participation Group, Universidad Nacional Autónoma de México, University of Arizona, University of Colorado Boulder, University of Illinois at Urbana-Champaign, University of Toronto, University of Utah, University of Virginia, Yale University, and Yunnan University. CA acknowledges the support of the Excellence Cluster ORIGINS, which is funded by the Deutsche Forschungsgemeinschaft (DFG, German Research Foundation) under Germany's Excellence Strategy – EXC-2094 – 390783311. SB acknowledges the National Agency for Research and Development (ANID) grant Gemini-32240014. RJA was supported by FONDECYT grant number 1231718 and by the ANID BASAL project FB210003. ALR acknowledges support from a Leverhulme Early Career Fellowship. YS acknowledges support from NSF grants AST-2009947 and AST-2509424. CA acknowledges Mike Eracleous for the Fe II and Balmer Continuum and High Order templates used in `pPXF`. CA acknowledges the valuable discussions with Vardha Bennert and Matthew Temple regarding scaling relations, as well as with Rogério Riffel about stellar population fitting.

[4] https://github.com/sdss

References

Abazajian, K. N., Adelman-McCarthy, J. K., Agüeros, M. A., et al. 2009, ApJS, 182, 543
Abdurro'uf, Accetta, K., Aerts, C., et al. 2022, ApJS, 259, 35
Almeida, A., Anderson, S. F., Argudo-Fernández, M., et al. 2023, ApJS, 267, 44
Angthopo, J., Granett, B. R., La Barbera, F., et al. 2024, A&A, 690, A198
Aydar, C., Merloni, A., Dwelly, T., et al. 2025, A&A, 698, A132
Balmaverde, B., Capetti, A., Marconi, A., et al. 2019, A&A, 632, A124
Barquín-González, L., Mateos, S., Carrera, F. J., et al. 2024, A&A, 687, A159
Barth, A. J., Bennert, V. N., Canalizo, G., et al. 2015, ApJS, 217, 26
Barth, A. J., Pancoast, A., Bennert, V. N., et al. 2013, ApJ, 769, 128
Batiste, M., Bentz, M. C., Raimundo, S. I., Vestergaard, M., & Onken, C. A. 2017, ApJ, 838, L10
Bernal, S., Sánchez-Sáez, P., Arévalo, P., et al. 2025, A&A, 694, A127
Bernardi, M., Shankar, F., Hyde, J. B., et al. 2010, MNRAS, 404, 2087
Blanton, M. R., Bershady, M. A., Abolfathi, B., et al. 2017, AJ, 154, 28
Bolton, A. S., Schlegel, D. J., Aubourg, É., et al. 2012, AJ, 144, 144
Bongiorno, A., Merloni, A., Brusa, M., et al. 2012, MNRAS, 427, 3103
Boroson, T. A. & Green, R. F. 1992, ApJS, 80, 109
Bowen, I. S. & Vaughan, Jr., A. H. 1973, Appl. Opt., 12, 1430
Brunner, H., Liu, T., Lamer, G., et al. 2022, A&A, 661, A1
Buchner, J., Starck, H., Salvato, M., et al. 2024, A&A, 692, A161
Cappellari, M. 2023, MNRAS, 526, 3273
Cardelli, J. A., Clayton, G. C., & Mathis, J. S. 1989, ApJ, 345, 245
Cardoso, L. S. M., Gomes, J. M., & Papaderos, P. 2017, A&A, 604, A99
Dalla Bontà, E., Peterson, B. M., Grier, C. J., et al. 2025, A&A, 696, A48
Dawson, K. S., Schlegel, D. J., Ahn, C. P., et al. 2013, AJ, 145, 10
de Jong, R. S., Agertz, O., Berbel, A. A., et al. 2019, The Messenger, 175, 3
DESI Collaboration, Abdul Karim, M., Adame, A. G., et al. 2026, AJ, 171, 285
Dey, A., Schlegel, D. J., Lang, D., et al. 2019, AJ, 157, 168
Dwelly, T., Salvato, M., Merloni, A., et al. 2017, MNRAS, 469, 1065
Eisenstein, D. J., Annis, J., Gunn, J. E., et al. 2001, AJ, 122, 2267
Eisenstein, D. J., Weinberg, D. H., Agol, E., et al. 2011, AJ, 142, 72
Fabian, A. C. 2012, ARA&A, 50, 455
Förster Schreiber, N. M., Genzel, R., Newman, S. F., et al. 2014, ApJ, 787, 38
Gebhardt, K., Bender, R., Bower, G., et al. 2000, ApJ, 539, L13
Girardi, L., Bressan, A., Bertelli, G., & Chiosi, C. 2000, A&AS, 141, 371
Graham, A. W., Erwin, P., Caon, N., & Trujillo, I. 2001, ApJ, 563, L11
Gunn, J. E., Siegmund, W. A., Mannery, E. J., et al. 2006, AJ, 131, 2332
Guo, H., Shen, Y., & Wang, S. 2018, PyQSOFit: Python code to fit the spectrum of quasars, Astrophysics Source Code Library
Harrison, C. M. & Ramos Almeida, C. 2024, Galaxies, 12, 17

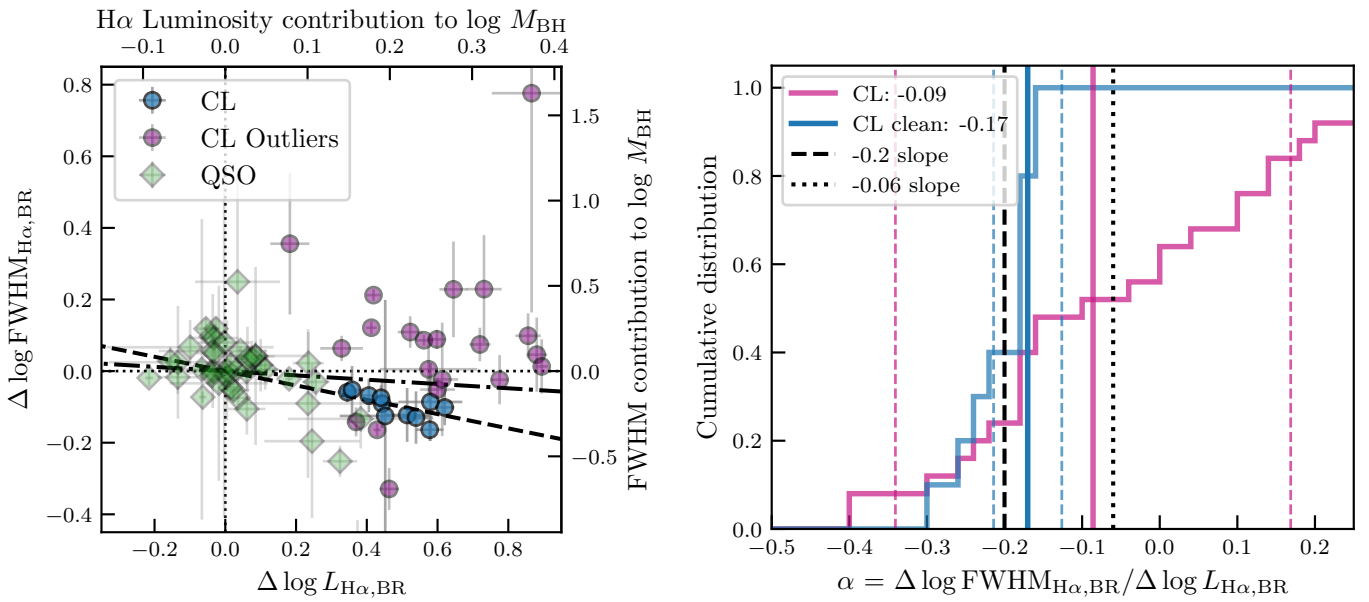

Fig. 18. Comparison of the difference in FWHM (y-axis) and luminosity (x-axis) of the broad component of Hα for two different observations of the same object. The left panel displays the difference of bright−dim for the CL sample (circles) and stack−individual spectra for the QSO sample (green diamonds). The objects from the CL sample that are within the standard deviation for the SMBH mass ratio from the "Clean" sample in Fig. 11 are shown in blue, while the outliers that have larger differences in their SMBH mass estimates are displayed in purple. The axes show the difference of the measured line property on the left and bottom, and their respective contributions to the black hole mass according to Eq. 3 on the right and top. The left and bottom axes have the same range, so the comparison in dex is straightforward. The (vertical and horizontal) dotted lines indicate the no-difference cases. The dashed line indicates the $\alpha = \Delta \log \mathrm{FWHM}_{H\alpha,BR} / \Delta \log L_{H\alpha,BR} = -0.2$ slope expected for breathing according to Eq. 3, and the dotted-dashed line is the $\alpha = -0.06$ derived for Hα in Wang et al. (2020). The right panel shows the cumulative distribution of the α slope for the overall CL sample in pink, and for the CL sample without the outliers in blue. The median distributions of α are vertical lines and in the legend, with the standard deviation shown as dashed lines.

Holt, J., Tadhunter, C. N., González Delgado, R. M., et al. 2007, MNRAS, 381, 611
Ji, X., Maiolino, R., Ferland, G., et al. 2025, MNRAS, 541, 2134
Kollmeier, J. A., Rix, H.-W., Aerts, C., et al. 2026, AJ, 171, 52
Kormendy, J. & Ho, L. C. 2013, ARA&A, 51, 511
Koss, M., Trakhtenbrot, B., Ricci, C., et al. 2017, ApJ, 850, 74
Lauer, T. R., Tremaine, S., Richstone, D., & Faber, S. M. 2007, ApJ, 670, 249
Li, J., Silverman, J. D., Merloni, A., et al. 2024, MNRAS, 527, 4690
Li, J., Silverman, J. D., Shen, Y., et al. 2025, ApJ, 981, 19
Magorrian, J., Tremaine, S., Richstone, D., et al. 1998, AJ, 115, 2285
Merloni, A., Lamer, G., Liu, T., et al. 2024, A&A, 682, A34
Mobasher, B., Dahlen, T., Ferguson, H. C., et al. 2015, ApJ, 808, 101
Morganti, R. 2017, Frontiers in Astronomy and Space Sciences, 4, 42
Park, D., Barth, A. J., Ho, L. C., & Laor, A. 2022, ApJS, 258, 38
Park, D., Woo, J.-H., Treu, T., et al. 2012, ApJ, 747, 30
Predehl, P., Andritschke, R., Arefiev, V., et al. 2021, A&A, 647, A1
Pucha, R., Juneau, S., Dey, A., et al. 2025, ApJ, 982, 10
Reines, A. E. & Volonteri, M. 2015, ApJ, 813, 82
Ricci, C. & Trakhtenbrot, B. 2023, Nature Astronomy, 7, 1282
Riffel, R., Mallmann, N. D., Rembold, S. B., et al. 2023a, MNRAS, 524, 5640
Riffel, R. A., Storchi-Bergmann, T., Riffel, R., et al. 2023b, MNRAS, 521, 1832
Rodríguez-Merino, L. H., Mayya, Y. D., Coelho, P. R. T., et al. 2020, ApJ, 889, L31
Runco, J. N., Cosens, M., Bennert, V. N., et al. 2016, ApJ, 821, 33
Runnoe, J. C., Brotherton, M. S., & Shang, Z. 2012, MNRAS, 427, 1800
Salpeter, E. E. 1955, ApJ, 121, 161
Salviander, S., Shields, G. A., Gebhardt, K., & Bonning, E. W. 2007, ApJ, 662, 131
Santini, P., Rosario, D. J., Shao, L., et al. 2012, A&A, 540, A109
Schlafly, E. F. & Finkbeiner, D. P. 2011, ApJ, 737, 103
Schlegel, D. J., Finkbeiner, D. P., & Davis, M. 1998, ApJ, 500, 525
SDSS Collaboration, Adamane Pallathadka, G., Aghakhanloo, M., et al. 2025, AASJournals, submitted
Shen, Y. 2013, Bulletin of the Astronomical Society of India, 41, 61
Shen, Y., Grier, C. J., Horne, K., et al. 2024, ApJS, 272, 26
Shen, Y., Richards, G. T., Strauss, M. A., et al. 2011, ApJS, 194, 45
Smee, S. A., Gunn, J. E., Uomoto, A., et al. 2013, AJ, 146, 32
Speranza, G., Ramos Almeida, C., Acosta-Pulido, J. A., et al. 2024, A&A, 681, A63
Stasińska, G., Cid Fernandes, R., Mateus, A., Sodré, L., & Asari, N. V. 2006, MNRAS, 371, 972
Strauss, M. A., Weinberg, D. H., Lupton, R. H., et al. 2002, AJ, 124, 1810
Suh, H., Civano, F., Trakhtenbrot, B., et al. 2020, ApJ, 889, 32
Tadhunter, C. N., Dickson, R. C., & Shaw, M. A. 1996, MNRAS, 281, 591
Tamura, N., Takato, N., Shimono, A., et al. 2016, in Society of Photo-Optical Instrumentation Engineers (SPIE) Conference Series, Vol. 9908, Ground-based and Airborne Instrumentation for Astronomy VI, ed. C. J. Evans, L. Simard, & H. Takami, 99081M
Tremaine, S., Gebhardt, K., Bender, R., et al. 2002, ApJ, 574, 740
Tsuzuki, Y., Kawara, K., Yoshii, Y., et al. 2006, ApJ, 650, 57
Vazdekis, A., Koleva, M., Ricciardelli, E., Röck, B., & Falcón-Barroso, J. 2016, MNRAS, 463, 3409
Venturi, G., Cresci, G., Marconi, A., et al. 2021, A&A, 648, A17
Vestergaard, M. & Peterson, B. M. 2006, ApJ, 641, 689
Vestergaard, M. & Wilkes, B. J. 2001, ApJS, 134, 1
Wang, S., Shen, Y., Jiang, L., et al. 2020, ApJ, 903, 51
Worthey, G. 1994, ApJS, 95, 107
Wu, Q. & Shen, Y. 2022, ApJS, 263, 42
York, D. G., Adelman, J., Anderson, John E., J., et al. 2000, AJ, 120, 1579
Yu, Z., Zou, F., & Brandt, W. N. 2023, Research Notes of the American Astronomical Society, 7, 248
Zeltyn, G., Trakhtenbrot, B., Eracleous, M., et al. 2026, ApJ, 1002, 61
Zeltyn, G., Trakhtenbrot, B., Eracleous, M., et al. 2024, ApJ, 966, 85
Zenteno, A., Kluge, M., Kharkrang, R., et al. 2025, A&A, 698, A171

[1] Max Planck Institute for Extraterrestrial Physics, Gießenbachstraße 1, 85748 Garching, Germany
[2] Excellence Cluster ORIGINS, Boltzmannstrasse 2, D-85748 Garching, Germany
[3] School of Physics and Astronomy, Tel Aviv University, Tel Aviv 69978, Israel
[4] Departamento de Astronomía, Universidad de Chile, Camino el Observatorio 1515, Santiago, Chile
[5] Millennium Nucleus on Transversal Research and Technology to Explore Supermassive Black Holes (TITANS)
[6] Department of Astronomy, University of Illinois Urbana-Champaign, Urbana, IL 61801, USA
[7] Department of Astronomy, University of Washington, Box 351580, Seattle, WA 98195, USA
[8] Universidad Diego Portales, Instituto de Estudios Astrofśicos, Facultad de Ingeniería y Ciencias, Av. Ejército Libertador 441, Santiago, Chile
[9] Instituto de Alta Investigación, Universidad de Tarapacá, Casilla 7D, Arica, Chile
[10] Institute for Gravitation and the Cosmos, The Pennsylvania State University, University Park, PA 16802, USA
[11] Department of Astronomy & Astrophysics, 525 Davey Lab, The Pennsylvania State University, University Park, PA 16802, USA
[12] Department of Physics, 104 Davey Laboratory, The Pennsylvania State University, University Park, PA 16802, USA
[13] Space Telescope Science Institute, 3700 San Martin Drive, Baltimore, MD 21218, USA
[14] Departamento de Astronomía, Universidad de Concepción, Casilla 160-C, Concepción, Chile
[15] Institute for Astronomy, University of Edinburgh, Royal Observatory, Edinburgh EH9 3HJ, UK
[16] Department of Astronomy & Astrophysics, The Pennsylvania State University, University Park, PA 16802, USA
[17] National Center for Supercomputing Applications, University of Illinois Urbana-Champaign, Urbana, IL 61801, USA
[18] Department of Physics and Astronomy, University of Utah, 270 S. 1400 E. E2108, Salt Lake City, UT 84112, USA
[19] Instituto de Astronomía, Universidad Nacional Autónoma de México, A.P. 70-264, 04510, Mexico, D.F., México
[20] Leibniz-Institut für Astrophysik Potsdam (AIP), An der Sternwarte 16, 14482 Potsdam, Germany
[21] Instituto de Astrofísica de Canarias, 38205 La Laguna, Tenerife, Spain

Table A.1. Parameters and references for the `pPXF` templates for the continuum.

Template	Parameters	References
Stellar Population	Padova isochrone Salpeter IMF Ages: 0.0631, 0.0794, 0.1, 0.1259, 0.1585, 0.1995, 0.2512, 0.3162, 0.3981, 0.5012, 0.631, 0.7943, 1.0, 1.2589, 1.5849, 1.9953, 2.5119, 3.1623, 3.9811, 5.0119, 6.3096, 7.9433, 10.0, 12.5893, and 15.8489 Gyr Metallicities: -1.71, -1.31, -0.71, -0.4, 0.0, 0.22 [M/H] Velocity: -300 to 500 km s^{-1} Velocity dispersion: 10 to 500 km s^{-1} Skweness and Kurtosis: -0.3 to 0.3	Vazdekis et al. (2016)
Fe II pseudo-continuum	FWHM: 1000, 1200, 1400, 1600, 1800, 2000, 2400, 2800, 3400, 4000, 4800, 5800, 7000, 8400, 10000, and 11800 km s^{-1}	Boroson & Green (1992), Vestergaard & Wilkes (2001)
AGN Featureless Continuum	Power-law normalization: 5100 Å Power-law slope: -3.0 to 0.0	Bernal et al. (2025)
Balmer Continuum	Optical depth τ: 0.1 to 2.0	Bernal et al. (2025)
Balmer High-order emission	FWHM: 100 to 11000 km s^{-1}	Bernal et al. (2025)

Table A.2. Parameters and references for the `PyQSOFit` templates for the continuum.

Template	Parameters	References
Fe II pseudo-continuum	Normalization: 0 to 10^{10} FWHM: 1200 to 10000 km s^{-1} Velocity shift: -0.01 to 0.01 × c	Boroson & Green (1992), Vestergaard & Wilkes (2001), Tsuzuki et al. (2006), Salviander et al. (2007)
Power-law	Normalization: 0 to 10^{10} Å Slope: -3.0 to 2.0	
Third order polynomium	Unbounded	

Appendix A: Fitting parameters

Table A.3. Configurations for the emission line fit for `PyQSOFit`. Global fits on top and local fits on the bottom part of the table.

λ_0	Complex	λ_{min}	λ_{max}	Line	N_G	σ_i	σ_{min}	σ_{max}	v_{off}	v_{idx}	w_{idx}	f_{idx}	f_{val}
6732.67	Ha	6400	6800	SII6732	1	0.001	0.00023	0.0017	0.005	1	1	0	-
6718.29	Ha	6400	6800	SII6718	1	0.001	0.00023	0.0017	0.005	1	1	0	-
6585.28	Ha	6400	6800	NII6585	1	0.001	0.00023	0.0017	0.005	1	1	1	0.003
6564.61	Ha	6400	6800	Halpha_na	1	0.001	0.00023	0.0014	0.005	1	1	0	-
6564.61	Ha	6400	6800	Halpha_br	3	0.005	0.0014	0.03	0.01	0	0	0	-
6549.85	Ha	6400	6800	NII6549	1	0.001	0.00023	0.0017	0.005	1	1	1	0.001
5008.24	Hb	4630	5050	OIII5007c	1	0.001	0.00023	0.0017	0.006	1	1	1	0.003
5008.24	Hb	4630	5050	OIII5007w	1	0.003	0.00023	0.004	0.006	2	2	2	0.003
4960.30	Hb	4630	5050	OIII4959c	1	0.001	0.00023	0.0017	0.006	1	1	1	0.001
4960.30	Hb	4630	5050	OIII4959w	1	0.003	0.00023	0.004	0.006	2	2	2	0.001
4862.68	Hb	4630	5050	Hbeta_na	1	0.001	0.00023	0.0014	0.005	1	1	0	-
4862.68	Hb	4630	5050	Hbeta_br	3	0.005	0.0014	0.03	0.01	0	0	0	-
4685.68	Hb	4630	5050	HeII_na	1	0.001	0.00023	0.0014	0.005	1	0	0	-
4685.68	Hb	4630	5050	HeII_br	1	0.005	0.0014	0.03	0.01	1	0	0	-
2798.75	MgII	2700	2900	MgII_na	1	0.001	0.0005	0.0014	0.01	0	0	0	-
2798.75	MgII	2700	2900	MgII_br	2	0.005	0.0014	0.05	0.01	0	0	0	-
1908.73	CIII	1700	1970	CIII_br1	1	0.005	0.0014	0.05	0.015	3	0	0	0.01
1908.73	CIII	1700	1970	CIII_br2	1	0.005	0.0014	0.05	0.015	3	0	0	0.01
1892.03	CIII	1700	1970	SiIII1892	1	0.002	0.001	0.015	0.003	1	1	0	0.005
1857.40	CIII	1700	1970	AlIII1857	1	0.002	0.001	0.015	0.003	1	1	0	0.005
1816.98	CIII	1700	1970	SiII1816	1	0.002	0.001	0.015	0.01	2	2	0	0.0002
1750.26	CIII	1700	1970	NIII1750	1	0.002	0.001	0.015	0.01	2	2	0	0.001
1718.55	CIII	1700	1900	NIV1718	1	0.002	0.001	0.015	0.01	2	2	0	0.001
1549.06	CIV	1500	1700	CIV_br	3	0.005	0.0014	0.05	0.015	0	0	0	0.05

Table A.3: continued.

λ_0	Complex	λ_{min}	λ_{max}	Line	N_G	σ_i	σ_{min}	σ_{max}	v_{off}	v_{idx}	w_{idx}	f_{idx}	f_{val}
1640.42	CIV	1500	1700	HeII1640	1	0.001	0.0005	0.0017	0.008	1	1	0	0.002
1663.48	CIV	1500	1700	OIII1663	1	0.001	0.0005	0.0017	0.008	1	1	0	0.002
1640.42	CIV	1500	1700	HeII1640_br	1	0.005	0.0017	0.02	0.008	2	2	0	0.002
1663.48	CIV	1500	1700	OIII1663_br	1	0.005	0.0017	0.02	0.008	2	2	0	0.002
1402.06	SiIV	1290	1450	SiIV_OIV1	1	0.005	0.0014	0.05	0.015	1	1	0	0.05
1396.76	SiIV	1290	1450	SiIV_OIV2	1	0.005	0.0014	0.05	0.015	1	1	0	0.05
1335.30	SiIV	1290	1450	CII1335	1	0.002	0.001	0.015	0.01	2	2	0	0.001
1304.35	SiIV	1290	1450	OI1304	1	0.002	0.001	0.015	0.01	2	2	0	0.001
1215.67	Lya	1150	1290	Lya_br	3	0.005	0.0014	0.05	0.02	0	0	0	0.05
1240.14	Lya	1150	1290	NV1240	1	0.002	0.001	0.01	0.005	0	0	0	0.002
6376.27	Fe_OI	5690	6400	FeX6376	1	0.001	0.00023	0.0017	0.005	1	0	0	-
6300.30	Fe_OI	5690	6400	OI6300	1	0.001	0.00023	0.0017	0.005	1	0	0	-
6088.68	Fe_OI	5690	6400	FeVII6088	1	0.001	0.00023	0.0017	0.005	1	0	0	-
5877.25	Fe_OI	5690	6400	HeI_na	1	0.001	0.00023	0.0014	0.005	1	0	0	-
5877.25	Fe_OI	5690	6400	HeI_br	1	0.005	0.0014	0.02	0.01	1	0	0	-
4364.44	Hg_Hd	4000	4470	OIII4363	1	0.001	0.00023	0.0017	0.005	1	0	0	-
4341.68	Hg_Hd	4000	4470	Hgamma_na	1	0.001	0.00023	0.0014	0.005	1	1	0	-
4341.68	Hg_Hd	4000	4470	Hgamma_br	1	0.005	0.0014	0.02	0.01	1	0	0	-
4102.89	Hg_Hd	4000	4470	Hdelta_na	1	0.001	0.00023	0.0014	0.005	1	1	0	-
4102.89	Hg_Hd	4000	4470	Hdelta_br	1	0.005	0.0014	0.02	0.01	1	0	0	-
3968.59	NeIII_OII	3650	4000	NeIII3967	1	0.001	0.00023	0.0017	0.005	1	0	0	-
3869.85	NeIII_OII	3650	4000	NeIII3869	1	0.001	0.00023	0.0017	0.005	1	0	0	-
3759.99	NeIII_OII	3650	4000	FeVII3759	1	0.001	0.00023	0.0017	0.005	1	0	0	-
3728.48	NeIII_OII	3650	4000	OII3728	1	0.001	0.00023	0.0017	0.005	1	0	0	-
3426.86	NeV	3310	3480	NeV3426_na	1	0.001	0.00023	0.0014	0.005	1	1	0	-
3426.86	NeV	3310	3480	NeV3426_br	1	0.005	0.0014	0.01	0.01	0	0	0	-
3346.78	NeV	3310	3480	NeV3346	1	0.001	0.00023	0.0017	0.005	1	1	0	-
2423.59	CII	2300	2460	NeIV2422	1	0.001	0.00023	0.0017	0.01	0	0	0	0.002
2324.81	CII	2300	2460	CII2326	1	0.001	0.00023	0.0017	0.01	0	0	0	0.002
1034.76	OIV	1000	1060	OIV1035	1	0.002	0.001	0.01	0.005	0	0	0	0.002

Notes. Column 1 (λ_0) specifies the central wavelength in vacuum of each specified line, in Angstroms. Column 2 (Complex) indicates the complex of lines, meaning that the lines belonging to the same complex will be fit together due to their proximity in wavelength range. Columns 3 (λ_{min}) and 4 (λ_{max}) indicate the minimum and maximum wavelengths in Angstroms for the fit of that line complex, respectively. Column 5 (Line) shows the line component that is being fit. The suffixes '_br', '_na', 'c', and 'w' indicate broad, narrow, core, and wing components, respectively. Column 6 (N_G) indicates the number of Gaussians considered for the fit of the line. Columns 7 (σ_i), 8 (σ_{min}), and 9 (σ_{max}) display the initial, minimum, and maximum values of sigma, the Gaussian width of the line, expressed as the natural logarithm of wavelength in Angstroms. In this scale, the FWHM is calculated by $2.3 \times \sigma \times c$, where c is the speed of light in km s^{-1}. Column 10 (v_{off}) shows the velocity offset as $v_{off} = \ln(\lambda_0/\lambda)$. Column 11 ($v_{idx}$) is the tied velocity offset index, which sets fixed values of the velocity offset for all lines in the same line complex that have the same index. Column 12 (w_{idx}) is the tied width index. Column 13 (f_{idx}) is the tied flux index, and the ratio of the fluxes that have the same flux index within the same line complex is defined in Column 14 (f_{val}) with the fixed flux value.

Table A.4. Width and offset parameters of the emission line fitting with `PyQSOFit` from Table A.3 in km s^{-1}.

Line	FWHM$_{min}$ [km s^{-1}]	FWHM$_{max}$ [km s^{-1}]	v_{off} [km s^{-1}]
Most single narrow	160	1 200	1 500
Balmer, He, [Ne V] narrow	160	1 000	1 500
Hα, Hβ, He II broad	1 000	21 000	3 000
Hγ, Hδ, He I broad	1 000	14 000	3 000
[Ne V] broad	1 000	7 000	3 000
[O III] core	160	1 200	1 800
[O III] wing	160	2 800	1 800
Mg II narrow	350	1 000	3 000
Mg II broad	1 000	35 000	3 000

The continuum of `pPXF` fits was done with fewer details than the continuum fit of `PyQSOFit` due to some characteristics of the code, which performs a linear combination instead of the fitting of each parameter. Therefore, the AGN continuum component added to `pPXF` fit has a more simplistic approach to account for a general trend of the AGN contribution, while the `PyQSOFit` one is more detailed to provide the measurements of different components contributing to the AGN continuum emission. Table A.1 describes

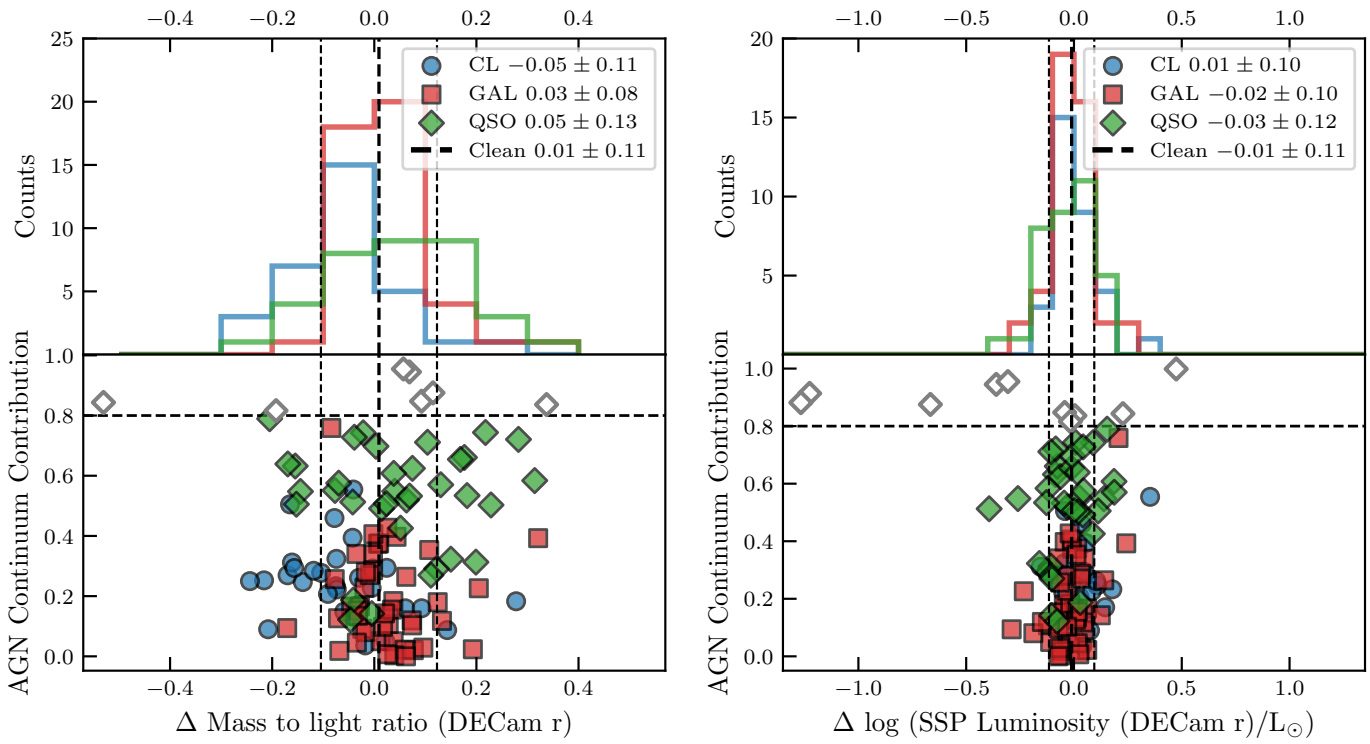

Fig. B.1. Difference of the mass-to-light ratio (left) and SSP luminosity (right), as in Fig. 5. Both are based on spectral flux integrated over the photometric DECam *r*-band coverage.

the parameters and references for the continuum fitting with `pPXF`, while Table A.2 does similarly for the continuum fitting using `PyQSOFit`.

The emission lines were fit with `PyQSOFit` using the parameters according to Table A.3. The set of lines at the top set of Table A.3 was fit together with the continuum and the fit for the whole wavelength range, while the set of lines at the bottom of the Table was fit locally due to being fainter and often absent. For completeness, we added all lines, though in our redshift range we do not fit lines with wavelengths smaller than Mg II. The same parameters are summarized in km s^{-1} in Table A.4. For the distinction between narrow and broad lines, we used the approximate value of FWHM= 1000 km s^{-1}. Some lines have a specific set of parameters (e.g., [O III] and [Ne V]) to avoid issues arising from possible blending.

Appendix B: Deriving stellar mass

The stellar mass is the direct product of the stellar luminosity and mass-to-light ratio (M/L). Since the luminosity depends linearly on flux, both measurements of the flux and of M/L carry similar weight in the calculation of stellar mass. The flux is integrated on the coverage of the *r* DECam band in the SSP spectral flux, while the M/L is an output from `pPXF` from the SSP analysis (also considering DECam *r* photometric band coverage).

From the Monte Carlo runs, the average statistical error in the flux (and luminosity) is dependent on the AGN contribution, ranging from 2% for the sample GAL to 12% for the sample QSO. Regarding the M/L, the average statistical uncertainty is 3-10% of the measurement, with lower values for the GAL sample than for the QSO sample. Therefore, both measurements have a similar stability in their statistical uncertainties after adding random noise.

To discuss and expand our estimates of the systematic uncertainties, we present the internal differences between the bright−dim and daily−allepoch observations for M/L and SSP luminosity in Fig. B.1. As expected, sample GAL has lower scatter in the internal comparison than sample QSO for both variables. We also emphasize the importance of the cut for sources with $f_{\rm AGN} > 0.8$, especially for the stellar luminosity, since this removes the main outliers from the QSO sample. Both the M/L and the SSP luminosity have an overall scatter (after removing objects with $f_{\rm AGN} > 0.8$) of 0.11 dex. However, since the offsets of each sample have different signs when comparing M/L and SSP luminosity (positive for the M/L and negative for luminosity for samples GAL and QSO, and negative for M/L and positive for luminosity for sample CL), the scatter of the stellar mass comparisons is larger than that of each individual component of its calculation (0.14 dex, as in Fig. 5).

Regarding the influence of the S/N on the results for the M/L and the SSP luminosity, we notice once again a stability of these methods, since both have a decrease of 0.01 dex when considering S/N > 5, and a decrease of 0.03 dex for S/N > 10. Therefore, the offset and scatter for S/N > 10 data is −0.01 ± 0.08 dex for M/L and 0.001 ± 0.07 for the SSP luminosity.

Summarizing the uncertainties in stellar mass estimates, the Monte Carlo analysis yields an average statistical uncertainty of 3% for sample GAL to 12% for sample QSO, similar to the results obtained for M/L and SSP luminosity, indicating that this is a robust measurement across runs with random noise applied to the same sources. However, because this robustness is not as tight when

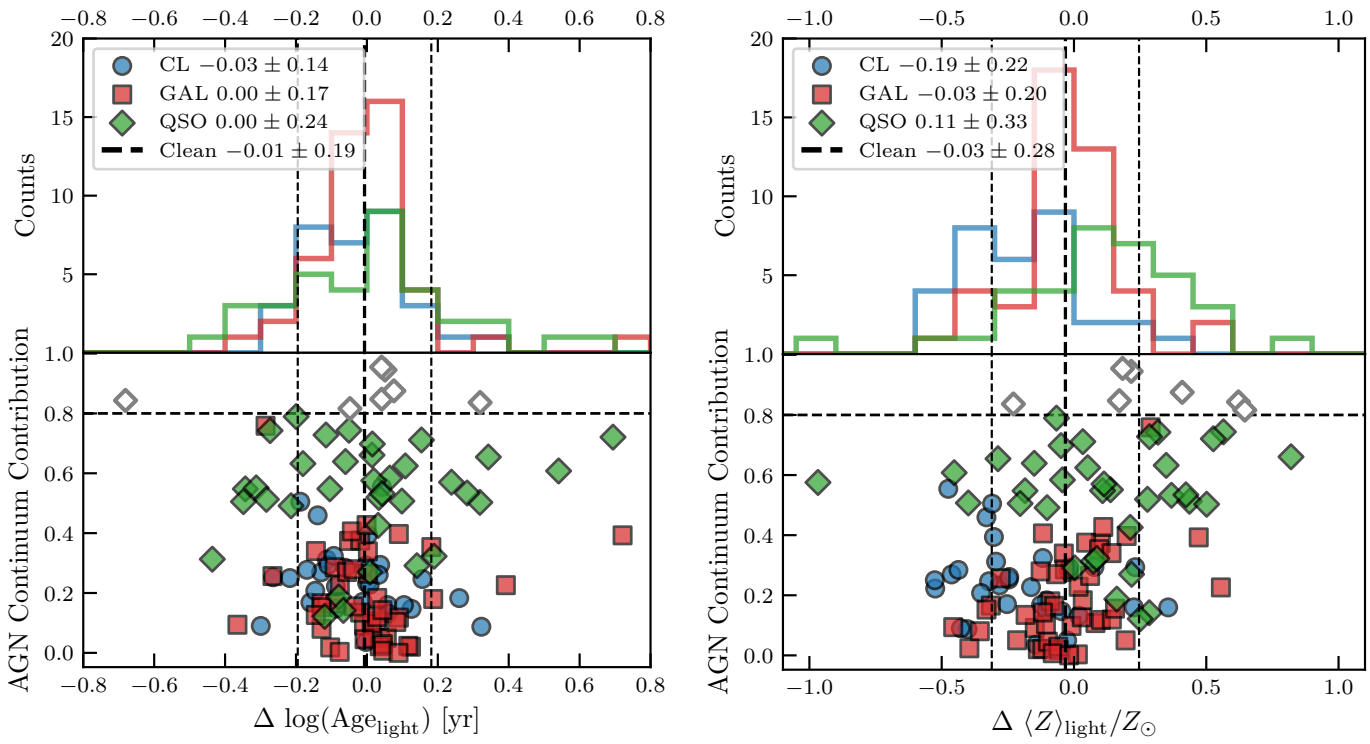

Fig. C.1. Difference of the average SSP light-weighted age (left) and metallicity (right), displayed as in Fig. 5. The bottom panel shows observations with $f_{\rm AGN} > 0.8$, marked with empty markers; these are excluded from the "Clean" statistics estimate.

comparing different observations of the same source, we argue that the systematic uncertainty of 0.14 dex obtained in the internal validation is more realistic than relying on the statistical uncertainty. The choice to use 0.14 dex as the uncertainty is also supported by external validation tests (see Fig. 7), which yielded 0.3-0.4 dex systematic differences across methods applied to the same sample.

Appendix C: The age-metallicity degeneracy

Reliably estimating the age and metallicity of stellar populations from optical data is complicated by the known degeneracy between these parameters, especially for old stellar populations (e.g., Worthey 1994; Rodríguez-Merino et al. 2020). Different combinations of age, metallicity, and dust can produce similar SEDs and spectral shapes; therefore, these properties will not be accurately measured unless the spectra have very high spectral resolution, S/N, and a large wavelength coverage (Angthopo et al. 2024). This degeneracy occurs because older populations, metal-rich stars, and dust all contribute to reddening the observed emission.

Figure C.1 shows the comparisons of the light-weighted average measurements of the age and metallicity for our samples. However, the interpretation of such plots should not be based solely on the dispersion since degeneracy could cause measurements from different observations to agree even if they are not accurate with respect to the object's stellar populations. This behavior is evident in the age distributions of spectra with $f_{\rm AGN} > 0.8$, with some cases showing dispersions of < 0.1 dex, although they remain associated with unreliable measurements of the host galaxy's properties. In such cases, in which the fit indicates a dominating AGN emission, the blue part of the continuum is assigned mainly to the AGN power-law featureless continuum, missing the contribution from young stellar populations (e.g., Tadhunter et al. 1996). Hence, the fit will miss the young stellar emission and assign high ages and metallicities to quasar-dominated spectra, indicating that the AGN outshines the stellar population rather than reflecting the host galaxy's true properties.

Despite the degeneracies mentioned above, improving the sample's S/N improves the results. For the age offset and scatter, considering S/N > 5 yields -0.01 ± 0.15, while for S/N > 10 we obtain -0.03 ± 0.13. For the metallicity, we have -0.06 ± 0.26 for a sample of S/N > 5 and -0.06 ± 0.21 for S/N > 10.

The fact that the quasar-dominated objects, which are in general bluer, will have their stellar populations estimated as redder, since the young population contribution will be attributed to the AGN power-law emission, enforces the recommendation of only trusting the host-galaxy properties for $f_{\rm AGN} < 0.8$. We also emphasize that the output of pPXF provides the weights for all the 150 E-MILES SSPs considered for the fit; therefore, there is more information available regarding the contribution of stellar populations with different ages and metallicities than considering the averages alone.